Deformation Twinning in a Metal-Intermetallic System: Novel Paradigm for Designing Alloys with Exceptional Strength-Ductility Combination

Bharat Gwalani[a#], Sriswaroop Dasari[a], Vishal Soni[a], Abhinav Jagetia[a], Shivakant Shukla[a], Priyanshi Agrawal[a], Rajiv S. Mishra[a], Rajarshi Banerjee[a]

[a]Materials Science and Engineering, University of North Texas, Denton, TX 76207
[#]current address: Physcial and Computational Directorate, Pacific Northwest National Laboratory, 902, Battelle Blvd, Richland, WA 99354
Corresponding authors: bharatgwalani@my.unt.edu, raj.banerjee@unt.edu

Abstract:

Engineering applications of high strength alloys are often restricted due to their poor tensile elongation or ductility. Alloys with high yield strength typically exhibit limited strain-hardenability (the difference between tensile and yield-strengths), leading to reduced tensile ductility. Deformation twinning, resulting in high strain hardenability, can lead to enhanced tensile elongation in single phase solid solutions, including high entropy alloys (HEAs). However, alloy systems involving a solid solution matrix strengthened with an intermetallic phase do not exhibit deformation twinning, thus limiting their tensile ductility. We have successfully exploited deformation twinning in a novel HEA, strengthened using nano-lamellar ordered multi-component intermetallic precipitates, leading to an exceptionally high yield strength (~1630 MPa), good tensile ductility (~15%), and an ultimate tensile strength (~1720 MPa), ***higher than any other reported fcc based alloy***. Exploiting deformation twinning in a two-phase metal-intermetallic system, offers a new paradigm for addressing the strength-ductility trade-off plaguing alloy design.

The ever-growing need for high strength metallic systems to support extreme environments for terrestrial as well as extra-terrestrial space requires radical changes in alloy development approaches. Alloys can be strengthened via several approaches, including grain-refinement, lattice straining, precipitation-strengthening employing a high-density of refined second phase(s), or multi-phase composite strengthening. The drawback is, in all cases a higher strength leads to a reduction in ductility and the formability of the alloy. Precipitation strengthening is an effective strengthening mechanism, often without substantial loss of ductility. Recently, Yang et al. developed a novel multicomponent intermetallic nanoparticle based strengthening showing promise in developing high strength alloys that retain high ductility[1]. The idea of multiple principal elements resulting in high entropy alloys (HEAs) has been accepted widely across the materials research community to develop compositionally unbiased chemically complex alloys for extended tunability of properties. HEAs with concentrated mixtures of transition elements like Co, Cr, Fe, and Ni can provide optimum combinations of properties like strength-ductility, toughness, and corrosion resistance[2].The stacking fault energy (SFE) of these alloys, which is another intrinsic property for structural alloys, is much lower as compared to Ni-base superalloys [3] however their specific strengths are typically much higher as compared to steels[4], which makes them very attractive for advanced applications. The most commonly investigated fcc-based CoCrFeNiMn HEA exhibits unusually high ductility and has a superior damage tolerance under cryogenic conditions[5]. Additionally, metastability of the parent fcc-phase leads to its stress-induced transformation to hexagonal closed-packed (hcp) phase in CoFeMnNi-base HEAs [6] leading to transformation induced plasticity, ensuring a high strain-hardenability thus enhanced tensile ductility. He et al. [7] studied effect of Ti and Al addition on the microstructure and mechanical properties of FeCoNiCr-based HEA by forming coherent nanosized $L1_2$ precipitates. The $L1_2$ (γ') precipitates offer the most promising precipitation hardening effects in fcc-based (γ) alloys, which forms the basis of high temperature Ni-base, Co-base, [8] and Al-base high temperature alloys[9]. Most optimal property combination was in $(FeCoNiCr)_{94}Ti_2Al_4$ alloy with tensile yield-strength ~ 900 MPa and ductility of 40%[7]. So far it has been very challenging to achieve high tensile strength of >1.5 GPa with a reasonable ductility in these alloys. Interestingly, bcc based HEAs such as based on WNbTaMoHf elements can exhibit extremely high compressive strength but typically have poor tensile ductility[10]. Ductility has been much more difficult to model due to the complex interplay between various deformation mechanisms. Hierarchical deformation

twinning, or multiple generations of twins, can accommodate more strain. Hence, deformation by twinning can be a potential mechanism to enhance strength-ductility synergy as increasing the number density of twin boundaries increases the strength as well as elongation, and strain hardenability of the material, via increasing dislocation storage capacity [11].

Here we used an iterative CALPHAD-based solution thermodynamic approach for alloy design, to create a precipitation-strengthened alloy based on the *fcc*-L1$_2$ architecture. The composition was optimized such that L1$_2$ phase is stable to 1150°C and volume fraction of L1$_2$ is greater than 35 % up to 1000°C. The starting point was the Al$_x$CoCrFeNi HEA system, which has been widely investigated[12]. We varied each of the elements iteratively to increase the phase fraction and high temperature stability of L1$_2$ phase. Figs. 1(a-b) show the first and last step while the complete iterations are provided in supplementary information). Our alloy composition (Al$_{0.2}$Ti$_{0.2}$Co$_{0.7}$CrFeNi$_{1.7}$) has a theoretical density of ~ 7.85 gm/cc (close to mild steel), expected maximum L1$_2$ phase fraction ~50 % and temperature stability ~1100°C (Fig. 1 (c)). The low Co and high Fe concentration in the alloy reduces the raw material cost compared to conventional Ni-base superalloys. The raw material cost of our alloy is estimated to be ~$5.5/lb whereas the cost of most commercial Ni-base superalloys lies in the range of $7-12$/lb based on current raw material cost[13]. Additionally, due to higher Fe concentration the SFE of the alloy is expected to be lower, thus enhancing the work hardenability and ductility of the alloy[3,4].

The optimized alloy composition was arc-melted and subsequently thermo-mechanically processed to achieve average *fcc* grain sizes of 30± 0 µm, 1.1±0.24 µm, and 0.67±0.20 µm, for the three conditions, CR-HTA-800, CR-800, and CR-600, respectively (Figs. 2 (a-d)). Annealing the severely cold worked alloy directly at aging temperatures results in concurrent recrystallization of *fcc* grains and precipitation of the strengthening phase (L1$_2$), limiting grain growth. The high magnification images in the inset of Figs. 2 (a, b) show the size and morphology of the precipitates in CR-HTA-800 and CR-800 conditions, while Figs. 2 (c-d) show the grain size and precipitates in case of the CR-600 condition. A clear change in L1$_2$ precipitate morphology is noticed in CR-800 condition (Fig. 2 (b)), from lamellar near the grain boundaries to spherical within the grains, due to heterogenous discontinuous precipitation versus homogenous nucleation, respectively. The precipitation is completely lamellar in the refined *fcc* grains in CR-600 condition (Fig. 2 (d), highlighted by white arrow).

The engineering stress-strain plots of the three conditions (Fig. 2(e)) shows that CR-HTA-800 condition has a yield strength (YS) of ~980 MPa, ultimate tensile strength (UTS) of ~1420 MPa, and 22% plastic strain to failure. The CR-800 condition exhibited a YS of ~1370 MPa, UTS of ~1540 MPa, and 12% ductility. The CR-600 condition exhibited a rather remarkable strength-ductility combination with YS of ~1630 MPa, UTS of ~1720 MPa, and 15% ductility. The strength-ductility are both higher for CR-600 as compared to CR-800; overcoming the well-established strength-ductility trade-off paradigm (Fig. 2 (e)). All three conditions exhibit a distinct four-stage work-hardening response, which is very characteristic of a low SFE material (Fig. 2 (f))[14]. The constant work hardening rate in stage B (black arrows) has been often correlated to deformation twinning[15]. This alloy demonstrates an outstanding strength-ductility combination as shown in supplementary Fig. S4 where the YS vs elongation has been plotted for this alloy in comparison with various superalloys.

To understand the microstructural origin behind these excellent and wide-ranging mechanical properties, more detailed characterization was carried out on the CR-HTA-800 and CR-600 samples. TEM diffraction patterns from all the three conditions confirmed that the precipitates were ordered $L1_2$ precipitates. Dark field TEM images highlighting the $L1_2$ precipitates in CR-HTA-800 and CR-600 conditions, recorded using an ordered superlattice diffraction spot (encircled in the insets) are shown in Figs. 3 (a-b), respectively. Further the APT analysis shows the three-dimensional (3D) morphology, distribution, and compositions of these precipitates. An iso-concentration surface delineating the region with Al higher than 8 at. % has been used to demarcate the $L1_2$ precipitates in the 3D reconstructions shown in Figs. 3(c-d) for CR-HTA-800 and CR-600 conditions, respectively. The precipitates have a spherical morphology with an average diameter of ~50 nm in CR-HTA-800 condition, while a nano-lamellar morphology with ~10 nm average width in CR-600 condition. The nano-lamellar precipitation in CR-600 is a result of concurrent recrystallization of *fcc* grains coupled with $L1_2$ precipitation. The low temperature recrystallization limited *fcc* grain-growth, and discontinuous $L1_2$ precipitation initiating from the grain boundaries[16] dominates over the more commonly observed homogeneous $L1_2$ precipitation within *fcc* matrix grains (details in supplementary Fig. ST9). The composition profiles across the *fcc* /$L1_2$ interface are shown as proximity histograms in Figs. 3 (e-f) and the phase compositions have been listed in supplementary Table ST2.

Post-deformation microstructures exhibited a high fraction of deformation-twins and shear-bands (SEM-EBSD analysis of CR-HTA-800 sample in Fig. 4 (a)). TEM from one such twinned region (highlighted by box) is shown in Figs. 4 (b-d). The bright-field (BF) TEM image in Fig. 4 (b) further shows the presence of secondary twins within the primary deformation-twin. Secondary twins are also observed within the annealing twins after deformation (refer supplementary Fig. S10). The SAD patterns in Figs. 4 (c-d) were recorded on the primary twin-matrix boundary and primary twin-secondary twin boundary, respectively, and clearly show the respective *fcc* crystal rotations resulting from twinning. Similarly, the deformed sample of the CR-600 condition (after strain to failure) also showed a high density of nano-twins (Fig. 4 (e)) within the sub-micron *fcc* grains. Typically, twinning is not a dominant deformation mechanism in such fine-grained *fcc* microstructures [17]. The diffraction pattern shown as an inset in Fig. 4 (e) exhibits twinned reflections from both *fcc* matrix and $L1_2$, indicating that the deformation-twins pass through both. An atomic resolution TEM image of a twin plane is shown in Fig. 4 (f) and based on the image shown in Fig. 4 (g), the thickness of these twins can be assessed to be ~6 nm.

The excellent yield strength and strain hardening of this HEA stems from a combination of solid solution strengthening and grain-boundary strengthening (or Hall-Petch strengthening) within the compositionally concentrated *fcc*-matrix, coupled with homogenous precipitation of $L1_2$ phase. In the CR-HTA-800 condition this leads to a YS of ~950 MPa, a high strain-hardening rate resulting from hierarchical twinning resulting in a UTS of ~1400 MPa, and ~ 20% tensile ductility. The high degree of deformation twinning indicates that the SFE has been substantially lowered in the matrix due to preferential partitioning of high SFE elements, Al, Ti, and Ni, into the $L1_2$ precipitates[4,18]. The further enhanced YS (~1630 MPa) in CR-600 condition can be attributed to finer size of recrystallized *fcc* grains (Hall-Petch strengthening) coupled with the nano-lamellar nature of the $L1_2$ precipitates. The Hall Petch and precipitation strengthening are calculated separately for the alloy (refer Supplementary Fig. S13 and Table ST4) and k_{HP} (Hall Petch coefficient) is estimated to be ~516 MPa$(\mu m)^{0.5}$.

The twinning induced plasticity (TWIP) is important for high strain hardening rates observed in a variety of steels [4], titanium alloys [19], and more recently in single phase high entropy alloys[5,20]. However, typically twinning is not a dominant deformation mode at room temperature in *fcc*+$L1_2$ precipitation-strengthened alloys [21]. In this study, deformation twinning, resulting in the TWIP

effect, was observed in both coarse grained and ultra-fine-grained *fcc*+L1$_2$ conditions. Additionally, in the CR-600 condition, electron diffraction evidence indicates twinning in both the matrix as well as in the L1$_2$ precipitates. Such a TWIP effect in microstructures containing intermetallic precipitates has not been reported so far in room temperature deformation and observing it in a HEA indicates that the L1$_2$ precipitates in these alloys, could potentially exhibit enhanced tendency for twinning. Previously, SF fringes and isolated faults have been reported to form in L1$_2$ precipitates under high temperature creep deformation [21,22]. While the underlying rationale requires further investigation, it can be speculated that the complex site occupancies in these L1$_2$ precipitates within HEAs presumably leads to changes in the nature of bonding [23] and lowering of the anti-phase boundary (APB) energy, facilitating growth of extended dislocations into deformation twins [22,24].

In conclusion, we designed a new alloy first optimizing the composition for high precipitate fraction and high temperature stability using equilibrium thermodynamics. The thermomechanical treatments results in a nano-lamellar precipitation of L1$_2$ phase in a low SFE disordered *fcc* matrix. Our alloy offers a low-cost material with an extremely high specific strength of 218 MPa/g/cc. The specific strengths of Ni-base superalloys are <150 MPa/g/cc and most steels are <200 MPa/g/c[25]. These new-generation HEAs or complex concentrated alloys could lead to superior structural properties, which are of both great fundamental and applied importance for advanced engineering systems. Our strategy can also be feasibly applied to many other alloy systems, such as steels, nickel or cobalt-base superalloys, and HEAs, to achieve enhanced properties.

Figure captions

Figure 1: CALPHAD based alloy design strategy (a, b) isopleths showing phase stability as a function of temperature and (a) Al, (b) Ti in base alloy. (c) The phase fraction vs temperature of the optimized composition.

Figure 2: (a) SEM images from (a) CR-HTA-800, (b) CR-800 (c-d) CR-600 conditions. (e) The tensile engineering stress vs strain and (f) work-hardening plots for the three conditions.

Figure 3: Dark Field TEM micrograph showing $L1_2$ precipitates in (a) CR-HTA-800 and (b) CR-600 conditions. The APT results from (c, e) CR-HTA-800 and (d, f) CR-600 conditions

Figure 4: Post deformation results from (a-d) CR-HTA-800 and (e-h) CR-600.

References

1   Yang, T. *et al.* Multicomponent intermetallic nanoparticles and superb mechanical behaviors of complex alloys. *Science* **362**, 933-937 (2018).

2   Miracle, D. B. & Senkov, O. N. A critical review of high entropy alloys and related concepts. *Acta Materialia* **122**, 448-511 (2017).

3   Shang, S. L. *et al.* Temperature-dependent ideal strength and stacking fault energy of fcc Ni: a first-principles study of shear deformation. *J Phys-Condens Mat* **24**, doi:Artn 155402

10.1088/0953-8984/24/15/155402 (2012).

4   Lu, J. *et al.* Stacking fault energies in austenitic stainless steels. *Acta Materialia* **111**, 39-46, doi:10.1016/j.actamat.2016.03.042 (2016).

5   Gludovatz, B. *et al.* A fracture-resistant high-entropy alloy for cryogenic applications. *Science* **345**, 1153-1158, doi:10.1126/science.1254581 (2014).

6   Li, Z. M., Pradeep, K. G., Deng, Y., Raabe, D. & Tasan, C. C. Metastable high-entropy dual-phase alloys overcome the strength-ductility trade-off. *Nature* **534**, 227-+, doi:10.1038/nature17981 (2016).

7   He, J. Y. *et al.* A precipitation-hardened high-entropy alloy with outstanding tensile properties. *Acta Materialia* **102**, 187-196, doi:10.1016/j.actamat.2015.08.076 (2016).

8   Betteridge, W. & Shaw, S. Development of superalloys. *Materials science and technology* **3**, 682-694 (1987).

9   Marquis, E. & Seidman, D. N. Nanoscale structural evolution of Al3Sc precipitates in Al (Sc) alloys. *Acta materialia* **49**, 1909-1919 (2001).

10   Senkov, O., Wilks, G., Miracle, D., Chuang, C. & Liaw, P. Refractory high-entropy alloys. *Intermetallics* **18**, 1758-1765 (2010).

11   Christian, J. W. & Mahajan, S. Deformation twinning. *Progress in materials science* **39**, 1-157 (1995).

12   Chou, H.-P., Chang, Y.-S., Chen, S.-K. & Yeh, J.-W. Microstructure, thermophysical and electrical properties in AlxCoCrFeNi (0≤ x≤ 2) high-entropy alloys. *Materials Science and Engineering: B* **163**, 184-189 (2009).

13   Metal Miner. *metal and alloy procies*, <https://agmetalminer.com/metal-prices/> (March 2020).

14   Asgari, S., ElDanaf, E., Kalidindi, S. R. & Doherty, R. D. Strain hardening regimes and microstructural evolution during large strain compression of low stacking fault energy fcc alloys that form deformation twins. *Metall Mater Trans A* **28**, 1781-1795, doi:DOI 10.1007/s11661-997-0109-3 (1997).

15   El-Danaf, E., Kalidindi, S. R. & Doherty, R. D. Influence of grain size and stacking-fault energy on deformation twinning in fcc metals. *Metall Mater Trans A* **30**, 1223-1233, doi:DOI 10.1007/s11661-999-0272-9 (1999).

16   Williams, D. & Butler, E. Grain boundary discontinuous precipitation reactions. *International Metals Reviews* **26**, 153-183 (1981).

17   Meyers, M. A., Vohringer, O. & Lubarda, V. A. The onset of twinning in metals: A constitutive description. *Acta Materialia* **49**, 4025-4039, doi:Doi 10.1016/S1359-6454(01)00300-7 (2001).

18   Kumar, K., Sankarasubramanian, R. & Waghmare, U. V. Influence of dilute solute substitutions in Ni on its generalized stacking fault energies and ductility. *Computational Materials Science* **150**, 424-431 (2018).

19   Williams, D. N. Metallographic Evidence of Mechanical Twinning in an Alpha-Beta Titanium Alloy. *Nature* **177**, 436-436, doi:DOI 10.1038/177436a0 (1956).

20   Huang, S. *et al.* Twinning in metastable high-entropy alloys. *Nat Commun* **9**, doi:ARTN 2381

10.1038/s41467-018-04780-x (2018).

21   Diologent, F. & Caron, P. On the creep behavior at 1033 K of new generation single-crystal superalloys. *Mat Sci Eng a-Struct* **385**, 245-257, doi:10.1016/j.msea.2004.07.016 (2004).

22   Tian, C. G., Han, G. M., Cui, C. Y. & Sun, X. F. Effects of stacking fault energy on the creep behaviors of Ni-base superalloy. *Mater Design* **64**, 316-323, doi:10.1016/j.matdes.2014.08.007 (2014).

23   Ding, Q. Q. *et al.* Tuning element distribution, structure and properties by composition in high-entropy alloys. *Nature* **574**, 223-+, doi:10.1038/s41586-019-1617-1 (2019).

24   Unocic, R. R. *et al.* Mechanisms of creep deformation in polycrystalline Ni-base disk superalloys. *Mat Sci Eng a-Struct* **483-84**, 25-32, doi:10.1016/j.msea.2006.08.148 (2008).

25   Li, Q. *et al.* High-Strength Nanotwinned Al Alloys with 9R Phase. *Advanced Materials* **30**, 1704629 (2018).

Figures
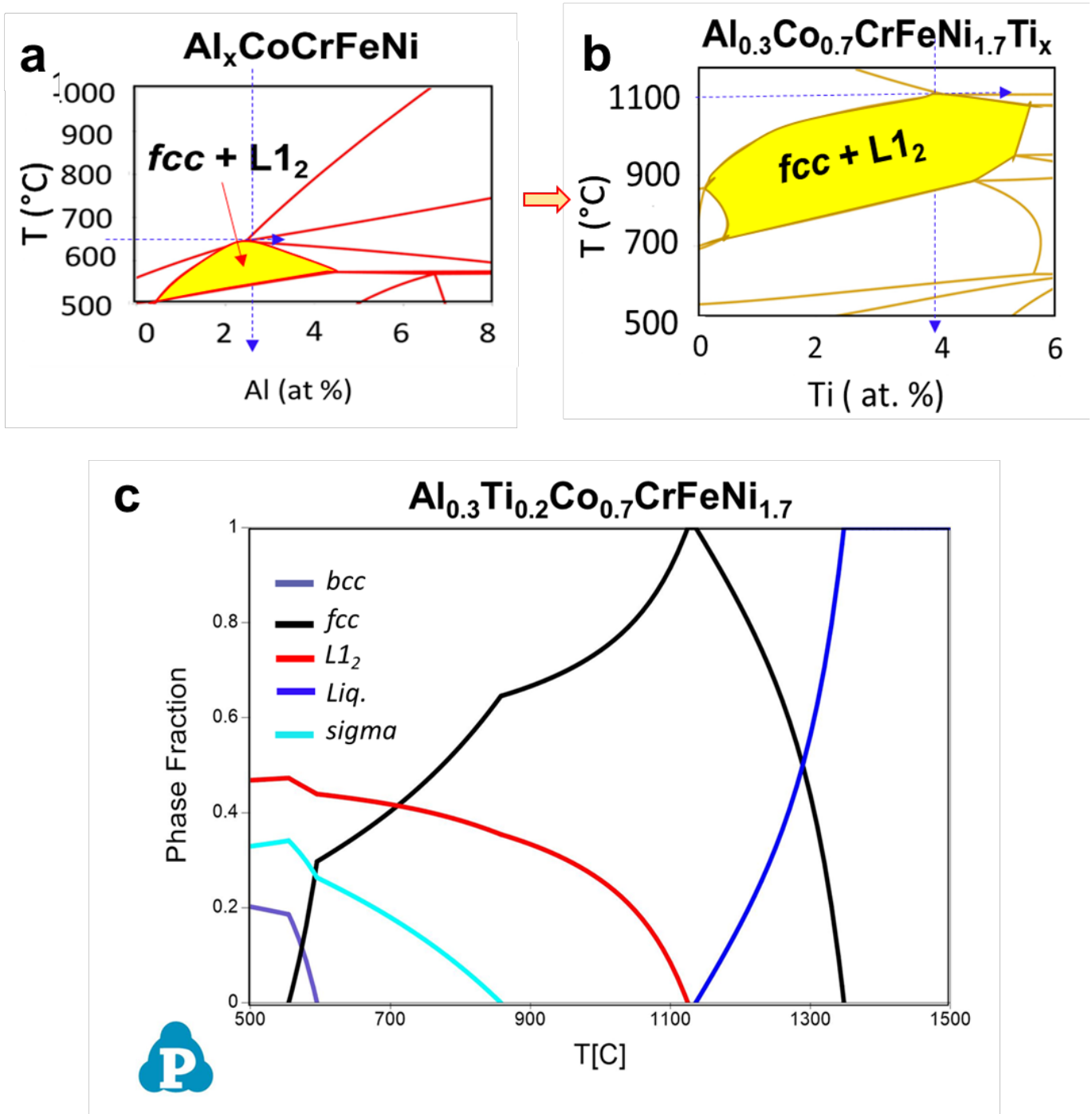
Figure 1: CALPHAD based alloy design strategy (a, b) isopleths showing phase stability as a function of temperature and (a) Al, (b) Ti in base alloy. (c) The phase fraction vs temperature of the optimized composition.
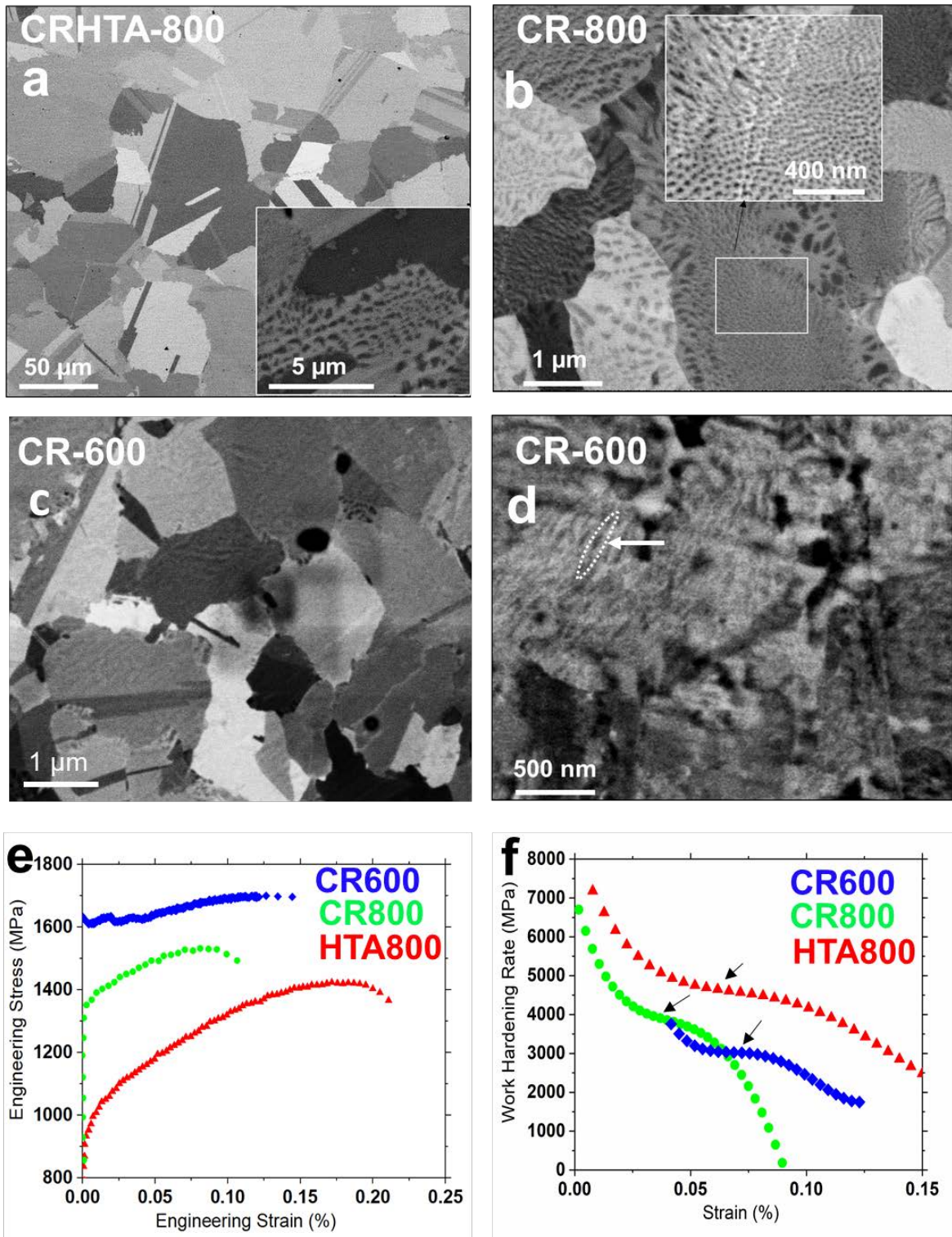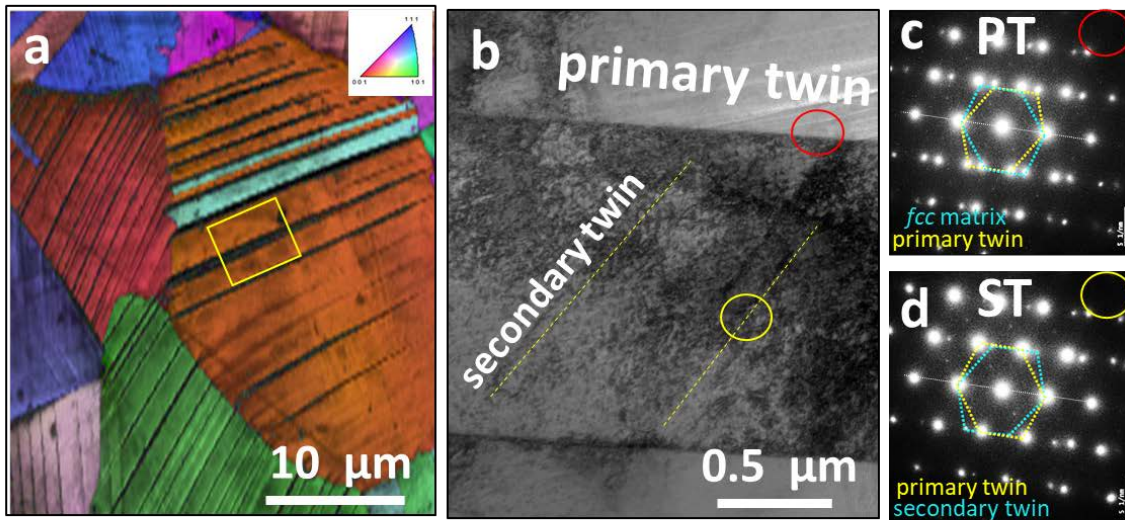
Figure 2: (a) SEM images from (a) CR-HTA-800, (b) CR-800 (c-d) CR-600 conditions. (e) The tensile engineering stress vs strain and (f) work-hardening plots for the three conditions.
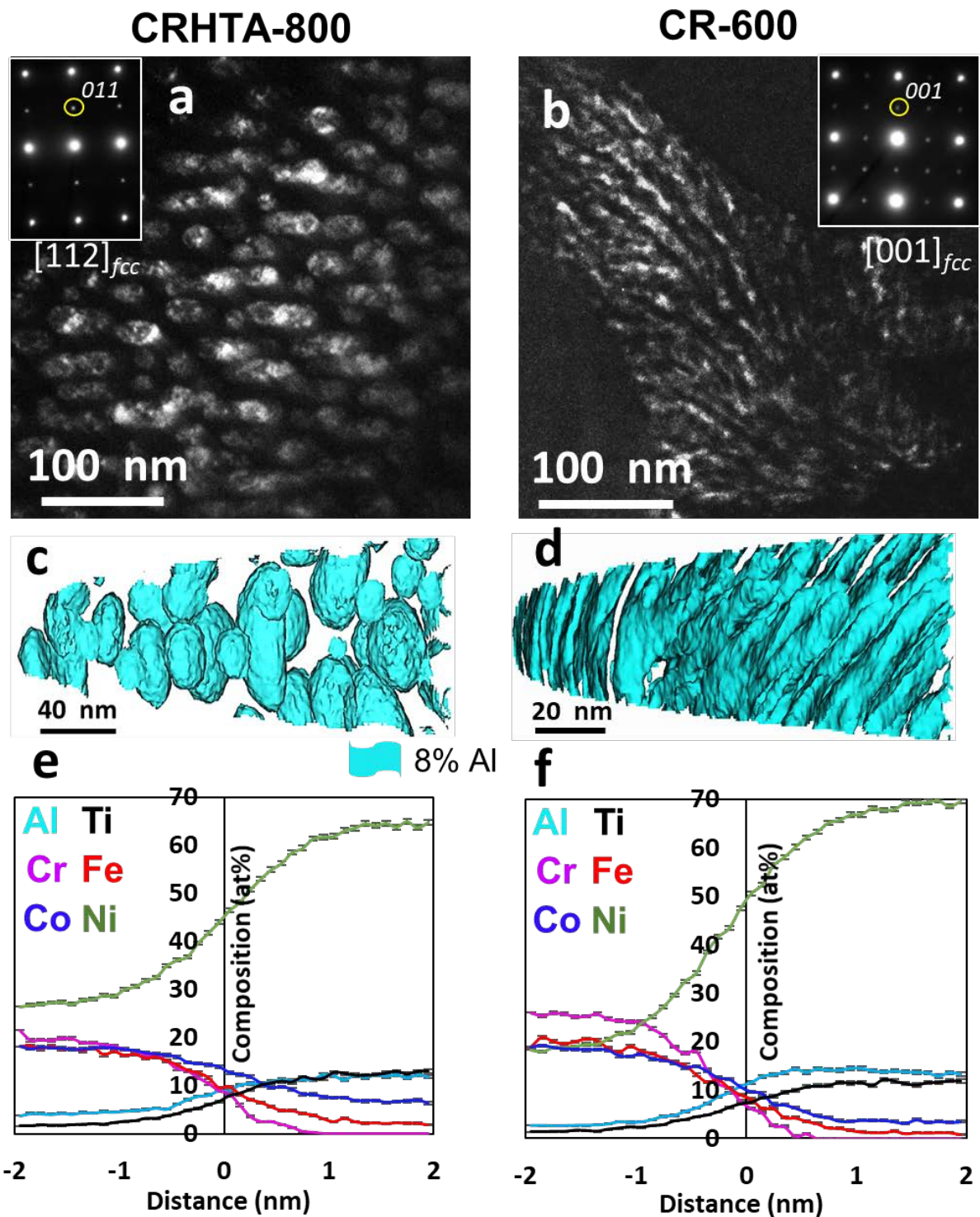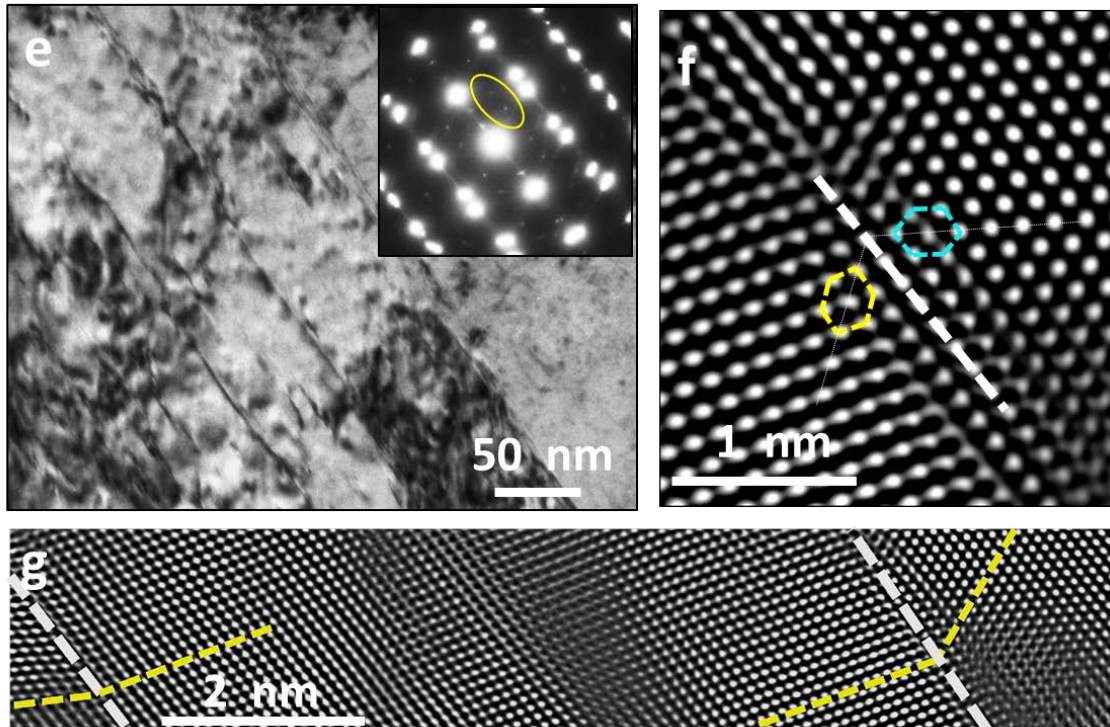
Figure 3: Dark Field TEM micrograph showing L1$_2$ precipitates in (a) CR-HTA-800 and (b) CR-600 conditions. The APT results from (c, e) CR-HTA-800 and (d, f) CR-600 conditions

CRHTA-800

CR-600

Figure 4: Post deformation results from (a-d) CR-HTA-800 and (e-g) CR-600.

Deformation Twinning in a Metal-Intermetallic System: Novel Paradigm for Designing Alloys with Exceptional Strength-Ductility Combination

Bharat Gwalani[a#], Sriswaroop Dasari[a], Vishal Soni[a], Abhinav Jagetia[a], Shivakant Shukla[a], Priyanshi Agrawal[a], Rajiv S. Mishra[a], Rajarshi Banerjee[a]

[a]Materials Science and Engineering, University of North Texas, Denton, TX 76207
 [#]current address: Physcial and Computational Directorate, Pacific Northwest National Laboratory, 902, Battelle Blvd, Richland, WA 99354
Corresponding authors: bharatgwalani@my.unt.edu, raj.banerjee@unt.edu

Materials and Methods

Thermodynamic modeling using CALPHAD

Addition of Al to Co, Cr, Fe, Ni based equiatomic HEA stabilizes $L1_2$ phase in the alloy. However, the phase fraction (<20 at. %) and solutionizing temperature (<600°C) for the $L1_2$ phase are reported to be low in this alloy system (*1*). Ni based superalloys have been developed from past five decades taking advantage of $L1_2$ based strengthenabilty, also due to increase in strengthening capability of $L1_2$ phase with rise in temperature. Hence, equilibrium stability of $L1_2$ at high temperature becomes critical. We used computational thermodynamic (CALPHAD) using TCHEA3 thermodynamic assessment from ThermoCalc (*2*) to simulate the change in the *fcc*+$L1_2$ phase field by varying the Al, Co, Cr Fe and Ni individually in the alloy. We noticed that minor addition of Ti enhanced the volume fraction and stability of $L1_2$ phase and hence, Ti was added to the HEA. The step by step iterative procedure to optimize the composition is provided in supplementary Fig. 1. We see that the optimum composition with respect to the concentration of each of these elements and $L1_2$ phase stability and volume fraction is reached at $Al_{0.2}Ti_{0.2}Co_{0.7}CrFeNi_{1.7}$. We than tested the calculated results by casting the alloy and conducting the microstructural characterization.

Materials Processing and Characterization

The alloy was cast in a conventional arc melting furnace by mixing constituent elements, with purity greater than 99.9%, on a water-cooled hearth made of copper in a controlled atmosphere of

pure argon. Repeated melting was carried out for five times and the ingot was inverted before every re-melt to ensure chemical homogeneity of the alloy. The cast ingot was ~10 mm in diameter and ~30 mm in length and was cut into thin slices for characterization. The as-cast samples were solution annealed (SA) at 1200°C for 1 hour and cold rolled (CR) by 80% reduction in thickness. Cold rolling followed by annealing resulted in recrystallized grain structure and improving compositional homogeneity. A third of the cold rolled alloy was annealed at 1100°C (high temperature annealing, HTA) to recrystallize followed by annealing at 800°C. This condition is called CR-HTA-800. Second part was cold rolled and directly annealed at 800°C, this called CR-800. And the remaining third part was directly annealed at 600°C after cold rolling, which is called CR-600 in the paper.

Macroscopic microstructural characterization and the composition of the arc melted materials was examined by using a FEI Nova-NanoSEM 230™ scanning electron microscope (SEM). The SEM was fitted with an energy dispersive X-ray (EDS) detector (EDAX, Model: Apollo X), and a pure Ni standard was used to calibrate it. Alloy samples were scanned several regions in areas of 1*1 mm2 to ensure the composition and homogeneity and EDAX's Genesis Spectrum version 6.0 software was used to process the raw data.

Conventional transmission electron microscopy (TEM) studies were carried out with a FEI Tecnai G2 TF20™ operating at 200 kV. Precipitate characterization was done using conventional and high angle annular dark field-scanning TEM (HAADF-STEM) modes. To measure the composition, energy dispersive spectroscopy (Super-X system) equipped on a FEI-TITAN G2 TEM microscope was used in the HAADF STEM mode operating at 300 kV and the results were analyzed with FEI's ES vision software version 6. TEM foils were prepared by a FEI Nova Nano lab 200 dual-beam focused ion beam (FIB) instrument using a Ga ion beam for milling. The ion beam thinning of the samples was done in multiple steps starting from 30 kV ions and finishing with 5 kV ions to reduce the surface damage caused by higher energy ions.

APT required the preparation of needle-shaped samples using the focused ion beam (FIB) method. The FIB-based site-specific specimen preparation was performed with a FEI instrument. The APT experiments were performed in a CAMECA LEAP 5000X XS system using the UV-laser pulse mode to achieve a reasonable yield. The analytical parameters were chosen by performing different test analyses. It was found that 100 pJ for the laser energy and 40 K for the base analysis

temperature offered a good compromise; minimizing local magnification effects while retaining a reasonable yield. The data were acquired at an average detection rate of 0.005 ions per pulse. The base pressure was maintained at less than 10^{-9} Pa during the analysis. Reconstruction of the acquired data was performed using the software IVAS 3.6.14 provided by CAMECA. This reconstruction was calibrated based on the initial tip curvature radius measured via SEM.

Mechanical Properties

Dog-bone-shaped tensile specimens with gauge length 3 mm were machined from the rolled and annealed sheets by Electrical Discharge Machining (EDM). Both sides of the specimen were ground using SiC paper to achieve final thickness of ~0.7 mm and gauge width of ~1.0 mm. Tensile tests were performed at an engineering strain rate of 10^{-3} s^{-1}. Each test was performed at least three times to ensure consistency; representative results are reported herein. These quasi-static tests used a LVDT (Linear Variable Displacement Transformer) extensometer to perform at least four independent tests to obtain tensile elongation and strength data. The elongation of the gauge length of each sample was measured after testing, and engineering stress–strain curves were calculated from the load-displacement data. Yield strength, ultimate tensile strength, and elongation to failure were determined from the uniaxial tensile stress–strain curves.

Deformation Twinning in a Metal-Intermetallic System: Novel Paradigm for Designing Alloys with Exceptional Strength-Ductility Combination

Bharat Gwalani[a#], Sriswaroop Dasari[a], Vishal Soni[a], Abhinav Jagetia[a], Shivakant Shukla[a], Priyanshi Agrawal[a], Rajiv S. Mishra[a], Rajarshi Banerjee[a]

[a]Materials Science and Engineering, University of North Texas, Denton, TX 76207

[#]current address: Physcial and Computational Directorate, Pacific Northwest National Laboratory, 902, Battelle Blvd, Richland, WA 99354

Corresponding authors: bharatgwalani@my.unt.edu, raj.banerjee@unt.edu

Supplementary Information

Section 1. CALPHAD based alloy design approach

Taking into account the compositional complexity of concentrated alloys like high entropy alloys (HEAs) and the number of possible combinations in five or six component space, optimization of alloy composition needs to be guided by computational modeling. We used an iterative CALPHAD-based solution thermodynamic approach (PANDAT (*1*) and Thermo-Calc(*2*)) for alloy optimization, employing the recently developed thermodynamic databases for HEAs, to create an ordered precipitation strengthened alloy, based on the *fcc*-$L1_2$ architecture. The composition was varied such that the ordered $L1_2$ phase is stable to 1150°C and volume fraction of $L1_2$ > 35 % up to 1000°C. The starting point of the alloy optimization was the $Al_xCoCrFeNi$ HEA system, which has been widely investigated(*3*). The *fcc* based alloys under this system can be strengthened by coherent ordered precipitates ($L1_2$), semi coherent ordered precipitates (B2), and exhibits a strong grain boundary strengthening effect(*4-6*). However, the ordered intermetallic $L1_2$ phase in this system is only stable at low temperatures, for example, in case of $Al_{0.3}CoCrFeNi$ the $L1_2$ phase is stable at temperatures lower than 600°C(*5*). Therefore, the principal aim of the iterative CALPHAD-based thermodynamic modeling was to increase the high temperature stability of the $L1_2$ phase and increase its volume fraction without the addition of high-density refractory elements. Co based superalloys have been developed in the past couple of decades which show high temperature $L1_2$ stability(*7*), but high Co increases the raw material cost. Hence, our current approach uses the high entropy concept to optimize the composition to make it economically feasible. Main Figs. 1(a) and (b) depict the isopleths derived from PANDAT using the PANHEA database(*1*), showing the first and last steps, respectively, of the composition optimization process. Comparing these two isopleths, the substantially larger *fcc*+$L1_2$ phase field in case of Fig. 1(b) is clearly visible. The complete set of iterations showing the effect of variation of each of the elements on phase stability is provided in the supplementary information in the form of isopleths (supplementary Fig. S1). We varied each of the elements iteratively to increase the phase fraction and high temperature stability of $L1_2$ phase.
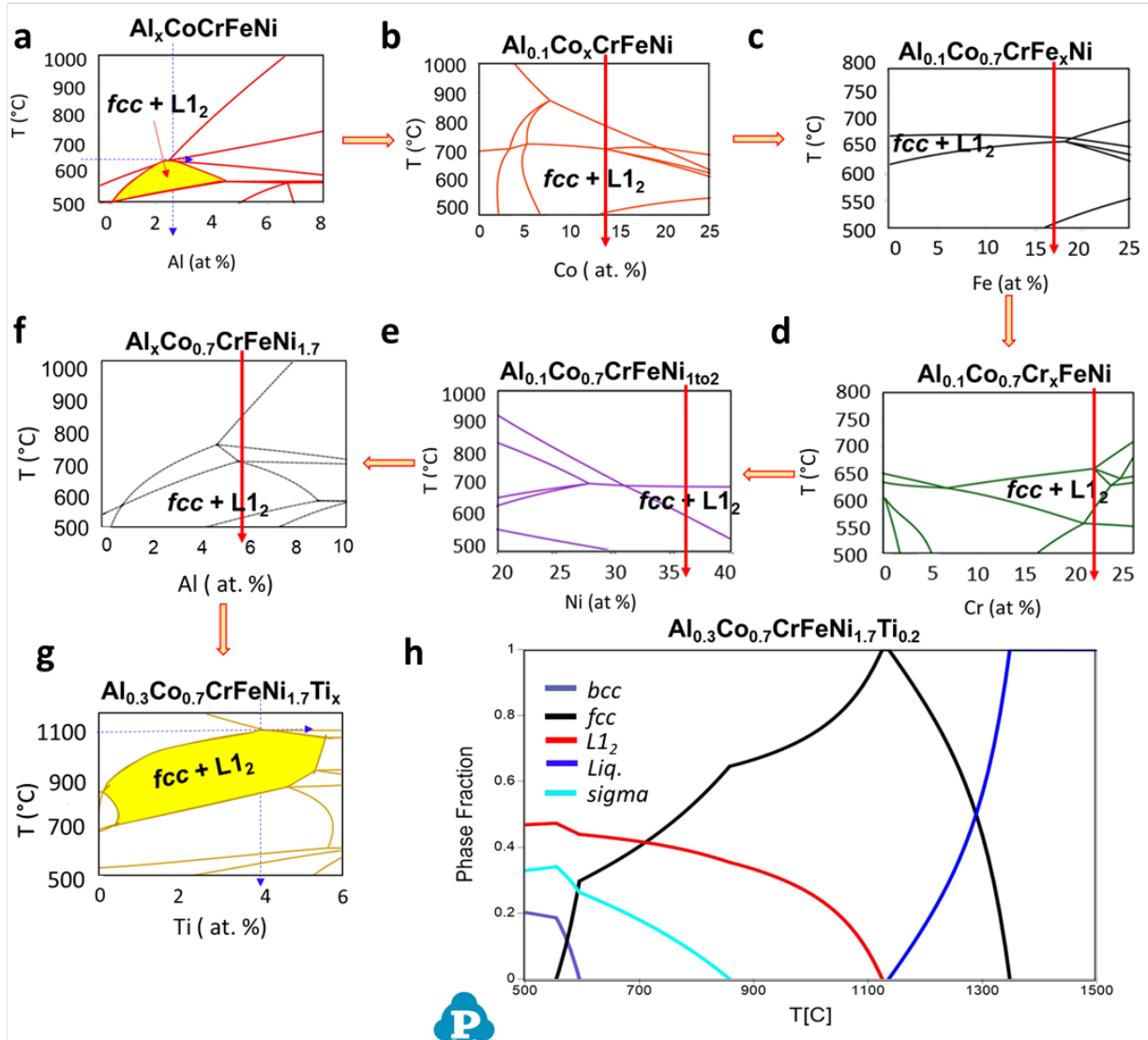
Supplementary Figure S1: We used an iterative CALPHAD-based solution thermodynamic approach, employing the recently developed thermodynamic databases for compositionally complex alloys like HEAs. PANHEA database developed by PANDAT was used to optimize the alloy composition to design a precipitation strengthened alloy based on an *fcc*-L1$_2$ architecture. The composition was varied such that the L1$_2$ phase is stable to >1100°C and volume fraction of L1$_2$ > 30 % up to 1000°C. (a) The isopleth showing the equilibrium phases at a function of temperature with variation of Al in CoCrFeNi alloy system. Note that the FCC+ L1$_2$ phases is stable to a maximum of 600 °C at Al concentration ~2.5 at. %. We use this concentration (2.5 at. %) to optimize the concentration of other elements to maximize the high temperature stability of L1$_2$ phase. (b-f) show the optimization of Co, Fe, Cr, Ni and then finally Al respectively. (g) Isopleth shows the equilibrium phases as function of temperature and Ti content. After several iterations it is noted that the stability of FCC+L1$_2$ phases is increased to ~1100 °C in an alloy with Al$_{0.3}$Ti$_{0.2}$Co$_{0.7}$CrFeNi$_{1.7}$ composition and the phase fraction of L1$_2$ >35% at 1000 °C.
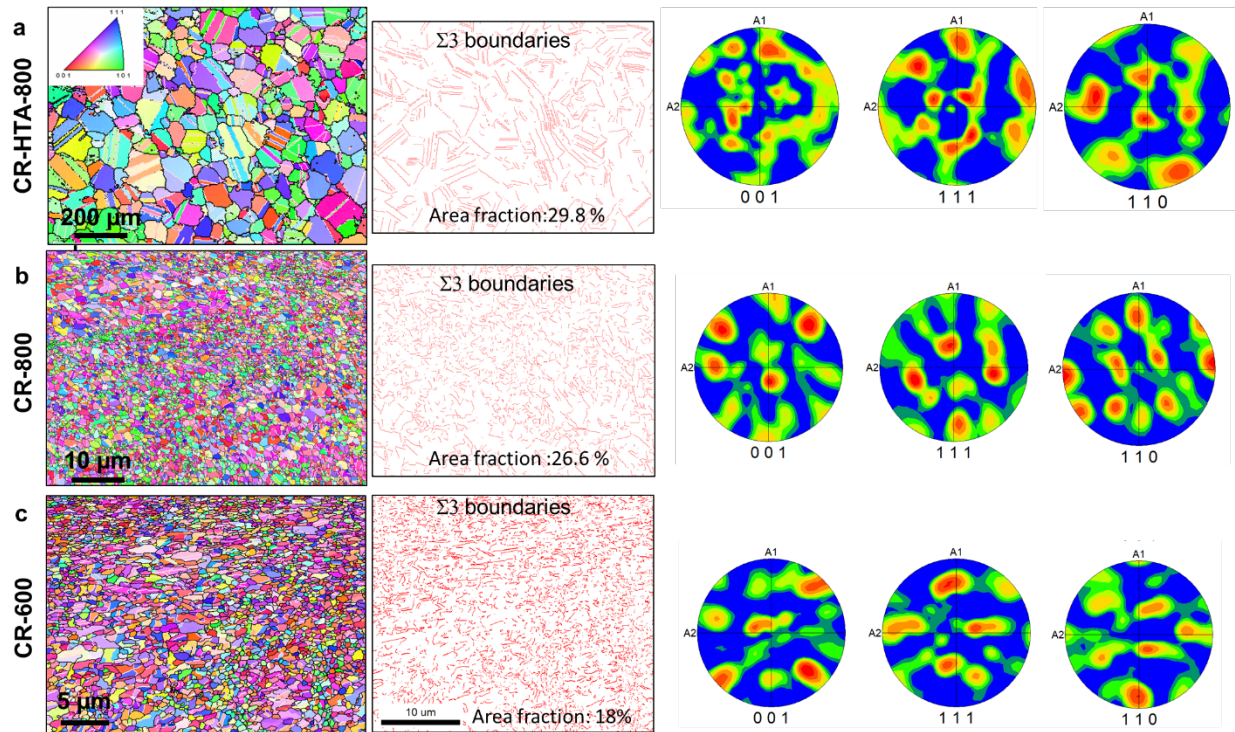
Supplementary Figure S2: Orientation image microscopy results from CR-HTA-800, CR-800, and CR-600 conditions. (a-c) pole figures along (001), (111), and (110) directions, inverse pole figure map and Ʒ3 boundaries highlighted by red boundaries in the CR-HTA-800, CR-800, and CR-600 heat treatment conditions respectively. The pole figure map shows that the recrystallized grains have random texture. The inverse pole figure shows the orientation maps with the grain size being 30± 10 µm in CR-HTA-800, 1.1± 0.24 µm in CR-800 and 0.67± 0.20 in CR-600 condition. The low energy Ʒ 3 boundaries in the three condition vary from 20 % to 30%.

Section 2. Mechanical Performance after thermomechanical processing
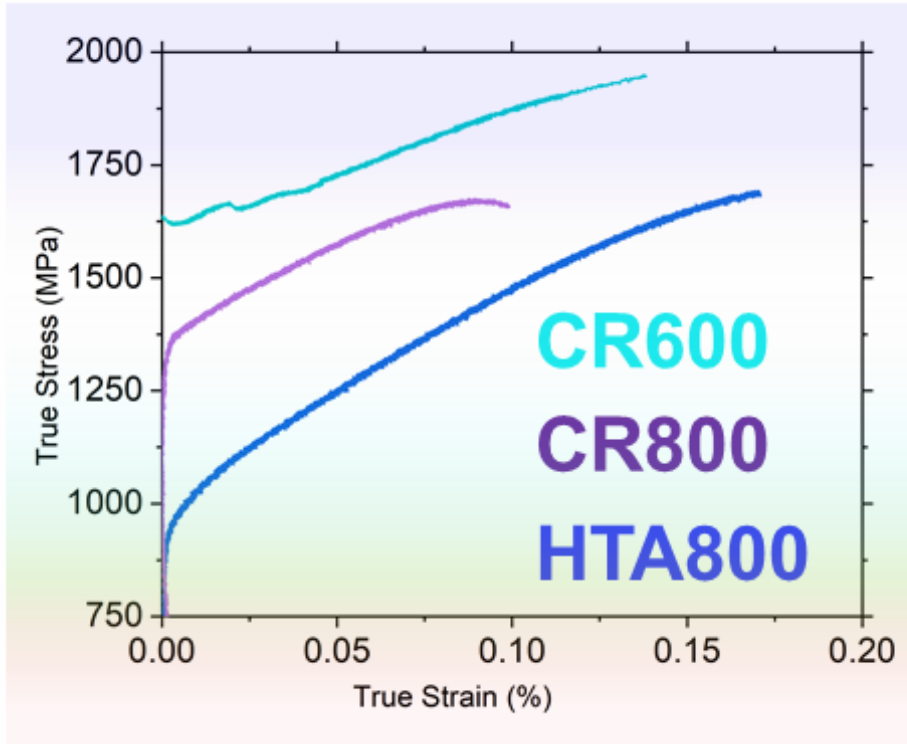
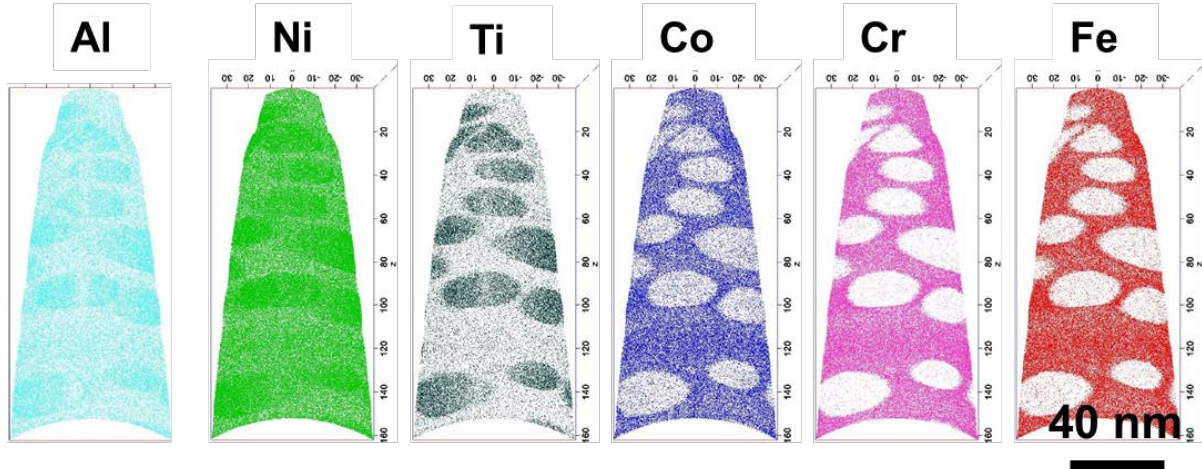**Supplementary Figure S3** showing the true stress-strain curves from the different heat treatment conditions

Supplementary Table S1: Hardness of various heat treatment conditions of the $Al_{0.3}Ti_{0.2}Co_{0.7}CrFeNi_{1.7}$ alloy

Condition	Average Hardness with Std. deviation (Hv)
As cast	311.12 ± 5.1
1100C-30min+88CR (as rolled)	501.71 ± 8.7
1100C-30min+88CR+1100C-2min	276.76 ± 9.4
1100C-30min+88CR+1100C-2min+800C-5hrs	371.56 ± 10.5
1100C-30min+88CR+800C-5hrs	451.89 ± 13.1
1100C-30min+88CR+600C-50hrs	540.46 ± 16.2
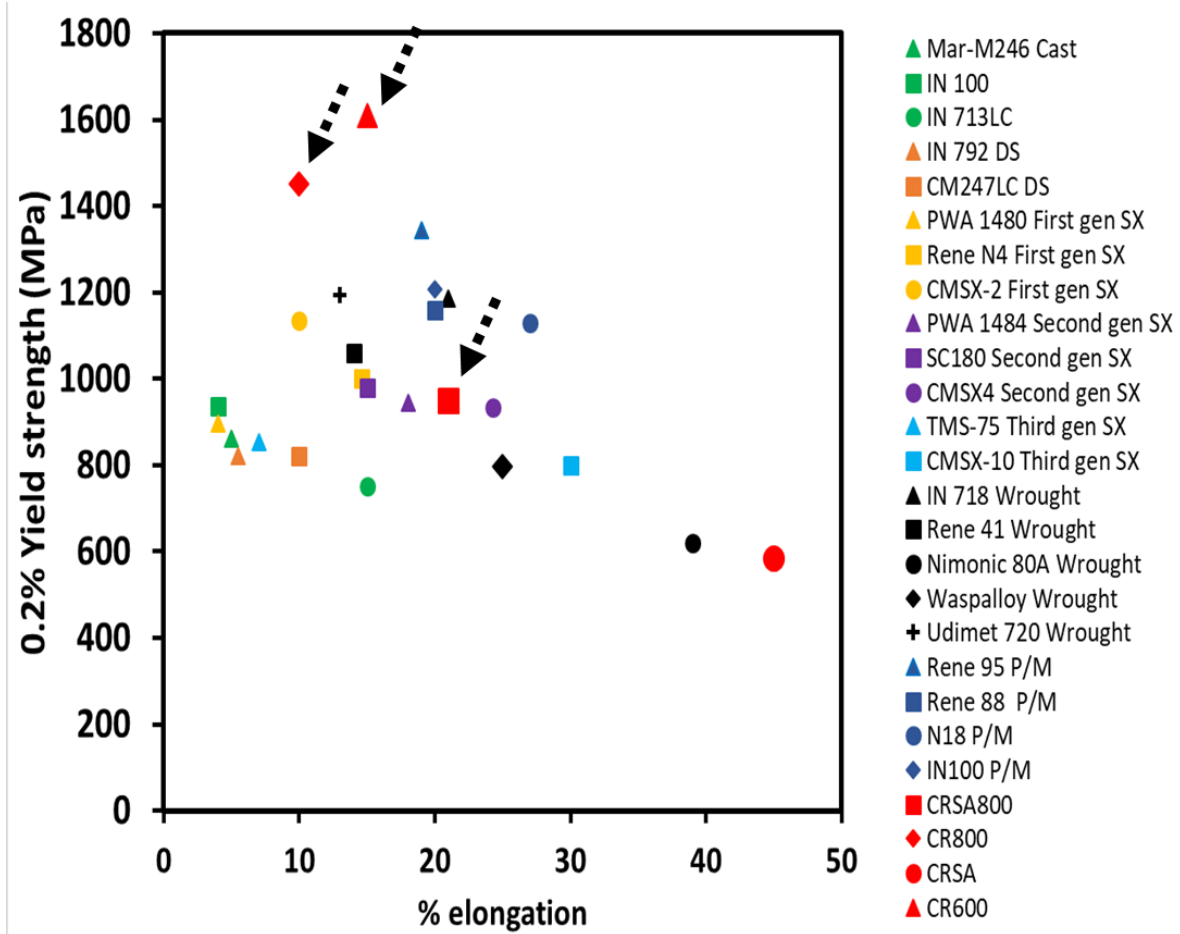
Supplementary Figure S4: An Ashby like plot comparing the yield strength vs percentage elongation of various Ni-based alloys, demonstrates the outstanding tensile properties of the current alloy. The CR-600 condition stands at the top of the chart where Ni-based superalloys from various generations and processing routes were plotted.

Section 3. Composition and distribution of ordered L1$_2$ precipitates

Supplementary Figure S5: Atom probe reconstructions showing the ion maps of various elements depicting the enrichment Al, Ti and Ni in the precipitate and Cr, Fe and Co in the matrix.
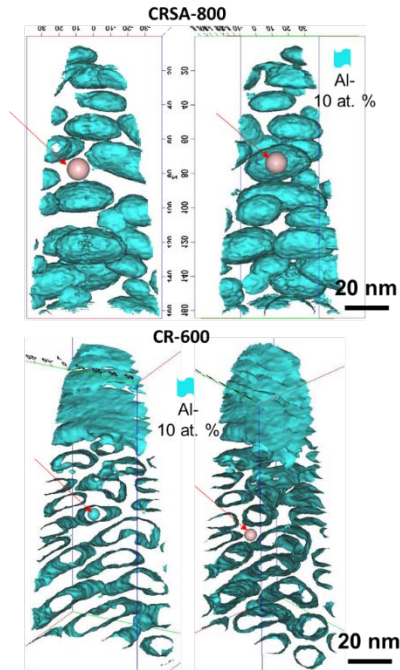
Supplementary Figure S6: Atom probe reconstructions where a cyan colored iso-concentration surface using the distribution of Al ions in the alloy is used to delineate the precipitate from the matrix. A red arrow marks a representative location of the region of interest (ROI) used for measuring the composition of each phase in the CR-HTA-800 and CR-600 conditions.

Table ST2: Composition of FCC and L1$_2$ phases from the HRSA-800 and CR-800 conditions from APT analysis.

Compositions from APT analysis

	Al	Co	Cr	Ni	Fe	Ti
CRHTA800						
FCC	4.82	21.61	22.12	30.11	19.43	1.91
L1$_2$	11.99	6.21	0.41	65.94	1.8	13.65
CR600						
FCC	2.75	21.19	30.21	19.64	24.8	1.39
L1$_2$	13.83	3.59	0	70.01	0.98	11.58

Note that the elemental distribution within FCC matrix and the ordered L1$_2$ precipitate is different for these two conditions. For examples the Cr content in the FCC matrix in case of the CR-600 (~30 at. %) condition is much higher than in case of the CR-HTA-800 condition (~22 at. %), the Ni content in L1$_2$ is higher in case of CR600 condition, while the Co content in L1$_2$ is lower in case of CR600. For a clear comparison, local composition from various locations (at least five locations in each case) within L1$_2$ and matrix were taken, an example of which is shown in supplementary Fig. S7. The average compositions are presented in Table ST3. The ordered L1$_2$ precipitates in CR-800 condition appears very similar to CR-HTA-800 (results from the CR-800 condition are presented in supplementary Fig. S8)
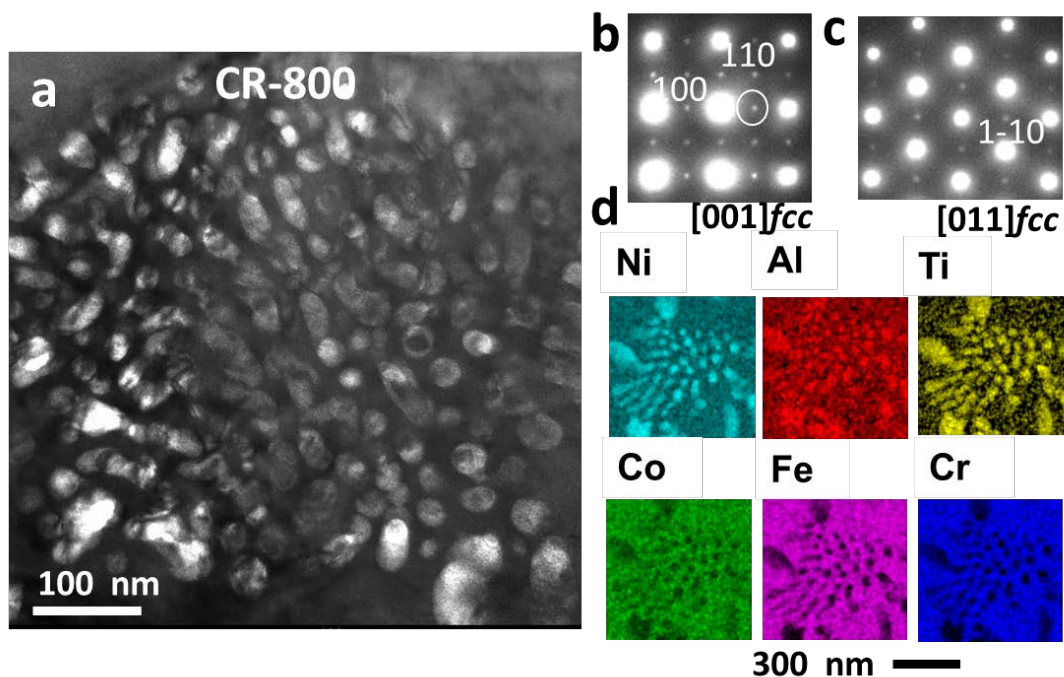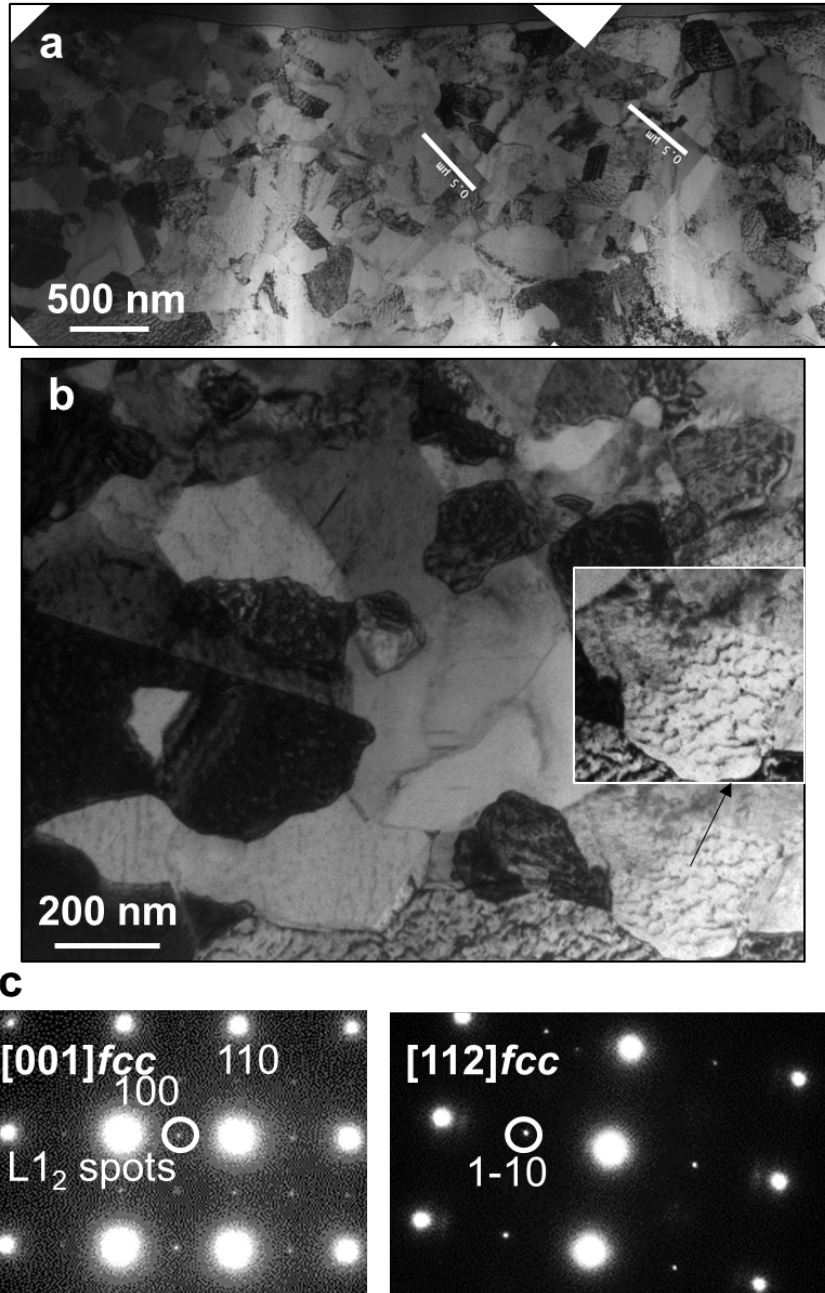
Supplementary Figure S7: TEM results from the CR-800 condition. (a) shows the dark field TEM images recorded by using a superlattice diffraction spot encircled in (b). The bright contrast ordered *fcc* precipitates can be clearly seen in the image. (b-c) selected area diffraction patterns after orienting the grain in [001] and [011] directions respectively. (d) Color coded elemental maps obtained by energy dispersive spectroscopy fitted in a TEM. The precipitates are enriched in Ni, Al and Ti while the matrix is rich in Cr, Fe and Co. The composition of the two phases is tabulated in Supplementary Table ST2.

Supplementary Table S3: composition of FCC and L1$_2$ phases measured using EDS in HAADF STEM mode from the HRSA-800 and CR-800 conditions.

Compositions from STEM EDS

|	Al	Co	Cr	Ni	Fe	Ti
CRHTA800						
FCC	4.01	20.14	27.82	24.76	22.55	0.72
L1$_2$	10.46	6.67	0.9	61.89	7.36	12.72
CR800						
FCC	1.89	18.66	24.82	27.36	26.14	1.13
L1$_2$	6.05	6.17	1.36	70.87	3.32	12.23

CR-600

Supplementary Figure S8: TEM results from CR-600 condition showing the bright field images and SAD patterns. The bright field TEM images in (a) shows the ultrafine grained structure and dark contrast nano-lamellar precipitates inside the grains are seen in (b). The selected area diffraction patterns recorded by orienting a single grain on [001] and [112] directions are shown in (c). The presence of superlattice spots on (001) and (011) locations unambiguously establishes the presence of ordered FCC phase (L1$_2$) in the matrix.

constructed across 8 at.%.

Nano-lammelar precipitation

When a supersaturated metastable FCC single solid solution phase is annealed at a temperature within a two-phase field containing the second strengthening phase (L1$_2$ in this case), the supersaturation of this solid solution can be relieved by a solid-state reaction that either involves homogenous precipitation or heterogenous precipitation. The nucleation of L1$_2$ precipitates occurring homogeneously throughout the matrix, termed as continuous precipitation (CP), typically results in a near spherical morphology of the precipitates. The heterogenous nucleation aided by a migrating grain boundary/reaction front results in a phenomenon called discontinuous precipitation (DP). One of the mechanisms of DP (Fig. 4), that is relevant to this study is called precipitation on migrating boundaries. The thermally activated motion of a grain boundary sweeps the solute in its path resulting in accumulation of solute at some points leading to the formation of L1$_2$ precipitate nuclei along the FCC grain boundary. The concentration gradient across the boundary drives further movement resulting in bowing out of the grain boundary due to pinning by precipitate nuclei. Simultaneously, the nuclei grow because of the accumulation of fresh solute from the migrating reaction front. This process repeats itself, ultimately leading to a microstructure consisting of colonies of alternating lamellar FCC + L1$_2$ phases. In the CR-HTA-800 condition which has undergone recrystallization at high temperature (1150°C) prior to annealing at 800°C, the starting condition consists of coarse FCC grains in which the grain boundary movement is limited. This results in a microstructure with mostly continuous precipitation, leading to a homogeneous distribution of L1$_2$ precipitates within the FCC matrix. In contrast, for the CR-600 condition, the 80% cold-rolled condition is directly annealed at a lower temperature of 600°C, resulting in concurrent recrystallization of the FCC grains and L1$_2$ precipitation within these grains. Therefore, as the FCC grains recrystallize, the resulting rapid motion of the grain boundaries sweeping the solute elements, is coupled with concurrent L1$_2$ precipitation at these boundaries. These precipitates grow themselves as well pin the boundaries, leading to discontinuous L1$_2$ precipitation, resulting in colonies of lamellar FCC+L1$_2$ permeating the entire microstructure.
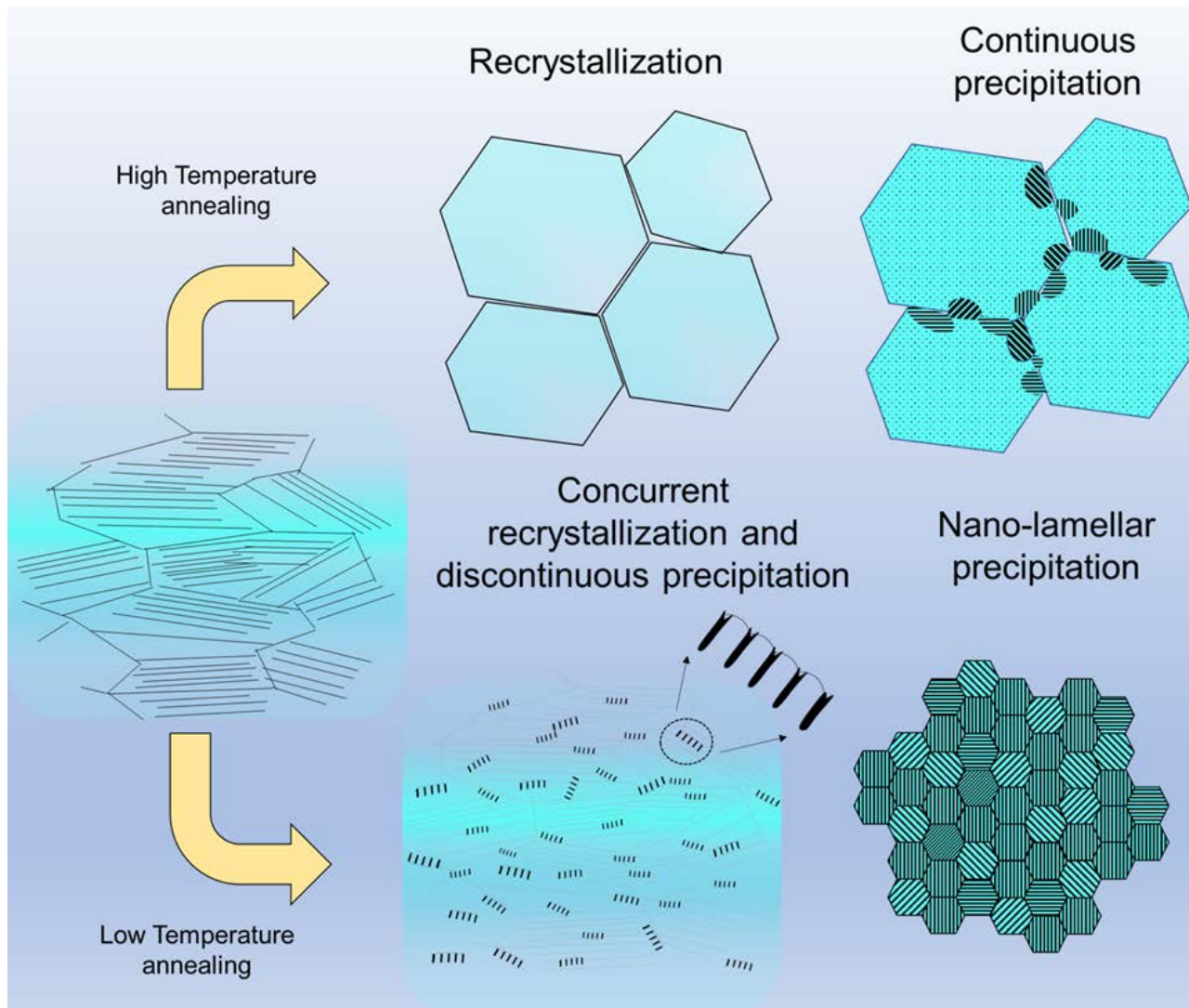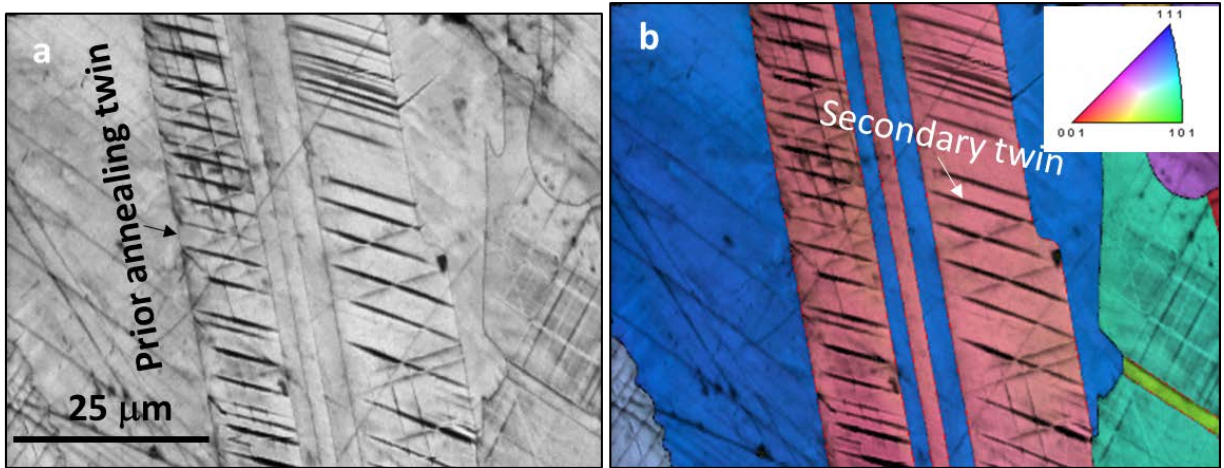
Supplementary Figure S9: Schematic showing the different modes of precipitation in two different heat treatments

## Section 4. Microstructure of Post Deformation conditions

Post-deformation microstructures were analyzed for a better understanding of the deformation mechanisms operative in this alloy. SEM-EBSD analysis (Fig. 4 (a)) of the CR-HTA-800 sample after tensile tested to failure showed a high fraction of deformation twins and shear bands. Along with shear bands traversing across the grains clearly seen in the inverse pole figure map over-lay with an image quality map, many lenticular twins are also captured. It should be noted that thinner deformation twins may not be properly indexed in Fig. 4(a).
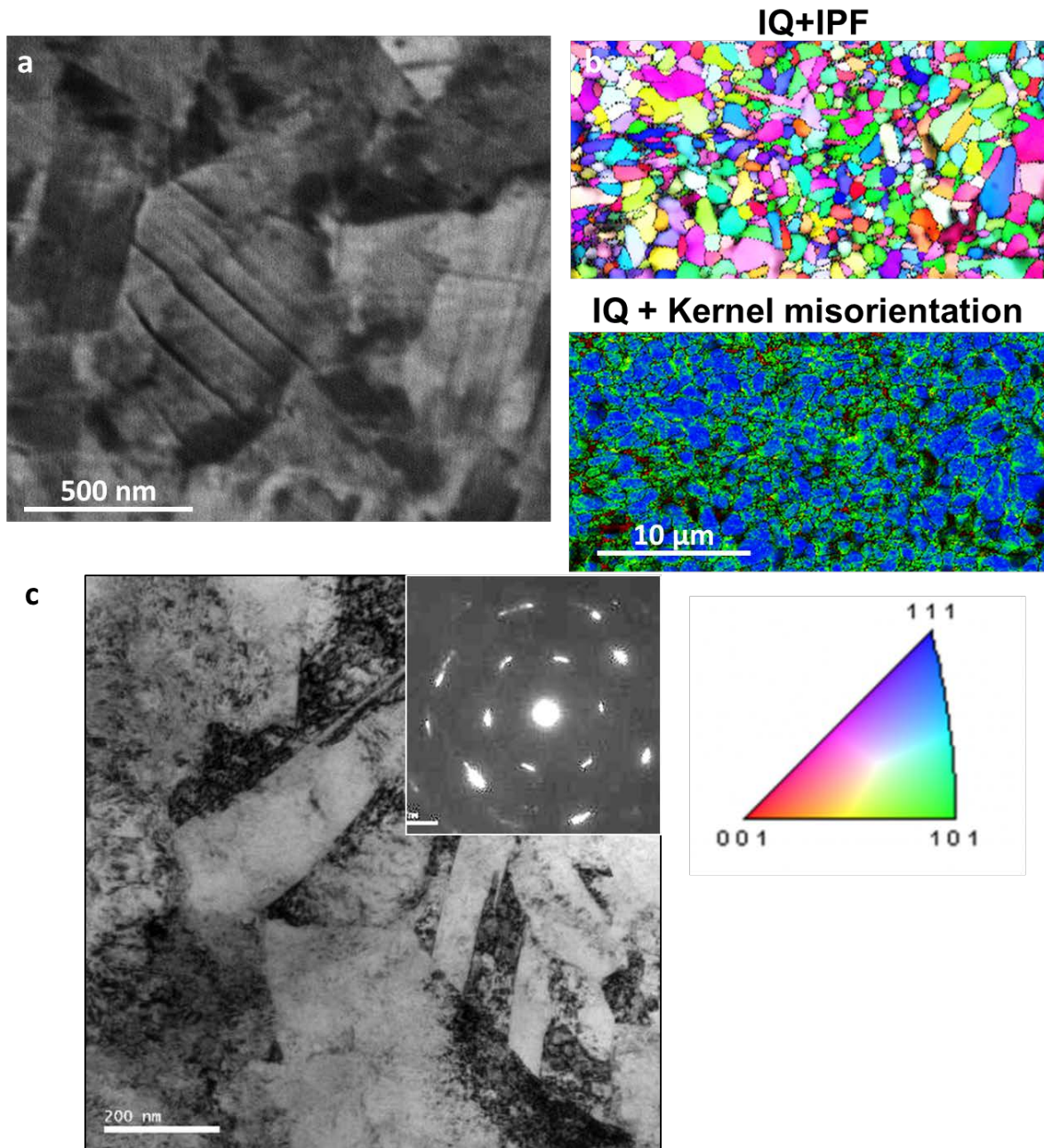

Supplementary Figure S10: Orientation image microscopy (OIM) results from the CR-HTA-800 condition after deformation to failure. (a) image quality (IQ) image showing the region of examination consisting of prior annealing twin (b) color coded overlay of IQ and IPF map shows the presence of secondary twins within the prior annealing twins. The presence of secondary and tertiary annealing twins suggests a low stacking fault energy of the alloy which can assist in work hardening and enhanced ductility.

CRHTA-800
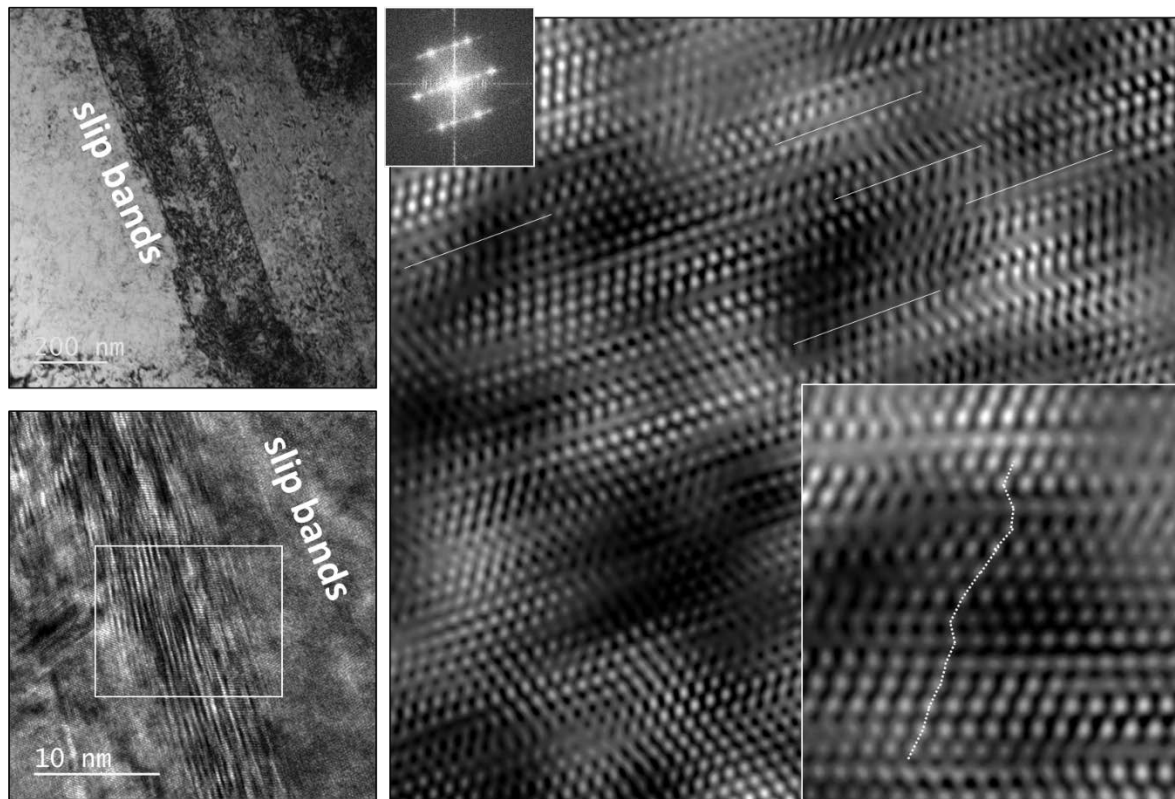
Supplementary Figure S11: High resolution TEM results from the CR-HTA-800 condition deformed to failure. The TEM samples was FIB lifted from a slip band and the high-resolution examination shows that the slip band consisted of multiple stacking faults and dislocations.

Supplementary Figure S12: SEM and TEM results from the CR-600 condition sample deformed to failure. (a) shows a high magnification SEM image showing the presence of deformation twinning the deformed microstructure. (b) OIM showing the IPF and kernel average misorientation maps depicting that the grain boundaries are the major stress concentration center for deformation. In nano-grained materials grain rotation and grain boundary sliding has been suggested to be an important deformation mechanism. However, in our current alloy, we notice a profuse amount of deformation twining as also seen in the BFTEM image in (c). Enhance deformation twinning is responsible for improvement in the room temperature ductility and high strength of alloy in this condition.

Section 5. Strengthening contributions from grain boundary and precipitation

The excellent yield strength and strain hardening of this HEA stems from a combination of solid solution strengthening and grain-boundary strengthening (or Hall-Petch strengthening) within the compositionally concentrated FCC matrix, coupled with homogenous precipitation of ordered $L1_2$ phase. In case of the CR-HTA-800 condition this leads to a high yield strength ~950 MPa, while retaining substantial deformation twinning in the FCC+$L1_2$ microstructure, leading to the high strain-hardening rate, an ultimate tensile strength ~1400 MPa, and tensile ductility ~ 20%. The high degree of deformation twinning in this condition indicates that the stacking fault energy has been substantially lowered in the matrix due to preferential partitioning of high stacking fault energy elements, Al and Ti, into the $L1_2$ precipitates(*8-10*). The further enhanced yield strength observed (~1630 MPa) for the CR-600 condition can be attributed to the finer size of recrystallized FCC grains (Hall-Petch strengthening) coupled with the nano-lamellar nature of the ordered $L1_2$ phase within these FCC grains. The Hall Petch strengthening was calculated separately for the FCC matrix (refer Supplementary Fig. S13 and Table S3) and k_{HP} (Hall Petch coefficient) is estimated to be ~516 MPa$(\mu m)^{0.5}$. The strengthening due to the ordered $L1_2$ phase in CRHTA-800 and CR-800 conditions, which have similar $L1_2$ phase fractions, is ~360 MPa while strengthening due the $L1_2$ phase in the CR-600 condition is ~480 MPa. The larger predicted phase fraction of $L1_2$ in CR-600 (40%) as compared to CR-800 (35%), could be the underlying reason for the higher contribution of this ordered phase to the yield strength in the former case. Additionally, the nano-lamellar nature of the $L1_2$ phase in the CR-600 condition potentially leads to further strength enhancement, though the underlying reasons need further investigation.

a CR-HTA   Avg. Grain size = 26± 9 µm

b

Engineering stress vs strain
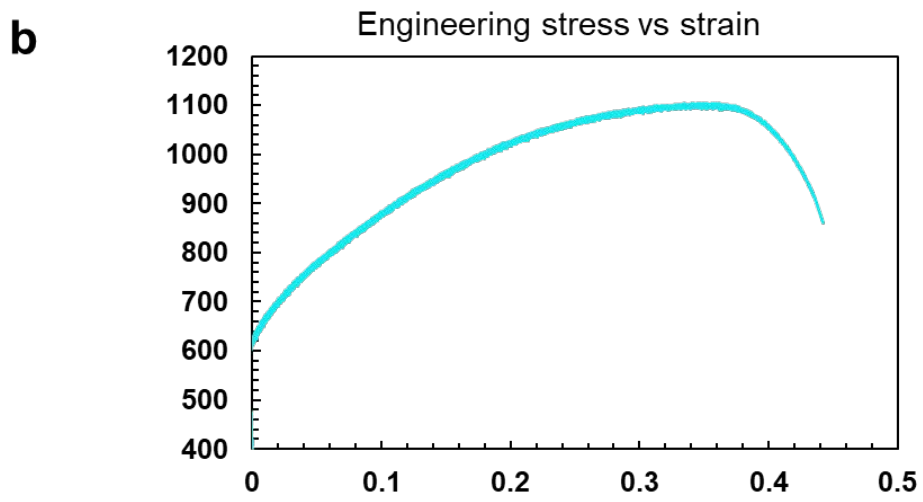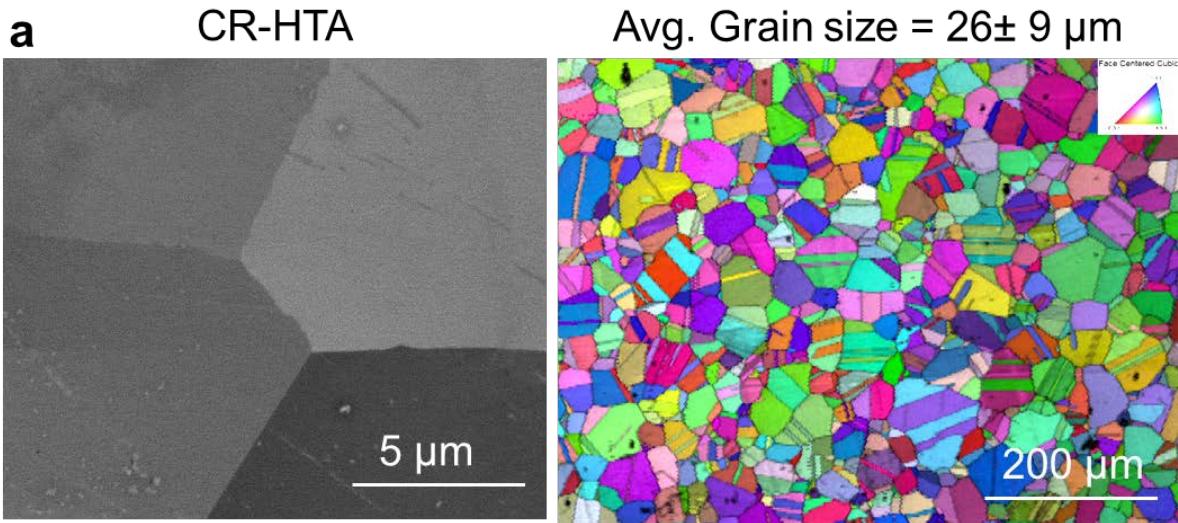
Supplementary Figure S13: (a) SEM and EBSD results from the CR-HTA condition. (b) Tensile engineering stress-strain curve from the same condition

Supplementary Table ST4: Grain boundary strengthening and precipitation strengthening contributions in different heat treatment conditions of the alloy.

Heat treatment condition	Grain size (µm)	Yield strength (MPa)	Grain boundary strengthening	Precipitate fraction	Precipitate Strengthening (MPa)
CR-HTA	26±9	620 MPa	σCR-HTA		
CR-HTA-800	30±10	980 MPa	620 Mpa (Similar grain size as CR-HTA)	35%	σCR-HTA-800 - σCR-HTA =360 MPa
CR-800	1.1±0.24	1370 MPa	σCR-HTA + σHP(CR-800) or σCR-800 - σppt(CR-800) =1010 MPa (Hence, σHP(CR-800) = 390 MPa and kHP = 516 MPa(µm)^0.5	Similar precipitate size and density as CR-HTA-800 35%	σCR-HTA-800 = 360 MPa
CR-600	0.67± 0.2	1630 MPa	σCR-HTA + σHP(CR-600) = 1150 MPa	40%	σCR-600 -σppt(CR-600) = 480 MPa

References

1. S.-L. Chen *et al.*, The PANDAT software package and its applications. *Calphad* **26**, 175-188 (2002).
2. J.-O. Andersson, T. Helander, L. Höglund, P. Shi, B. Sundman, Thermo-Calc & DICTRA, computational tools for materials science. *Calphad* **26**, 273-312 (2002).
3. H.-P. Chou, Y.-S. Chang, S.-K. Chen, J.-W. Yeh, Microstructure, thermophysical and electrical properties in AlxCoCrFeNi (0≤ x≤ 2) high-entropy alloys. *Materials Science and Engineering: B* **163**, 184-189 (2009).
4. D. Choudhuri, S. Shukla, B. Gwalani, R. Banerjee, R. S. Mishra, Deformation induced intermediate metastable lattice structures facilitate ordered B2 nucleation in a fcc-based high entropy alloy. *Mater Res Lett* **7**, 40-46 (2019).
5. B. Gwalani *et al.*, Modifying transformation pathways in high entropy alloys or complex concentrated alloys via thermo-mechanical processing. *Acta Materialia* **153**, 169-185 (2018).
6. B. Gwalani *et al.*, Optimizing the coupled effects of Hall-Petch and precipitation strengthening in a Al0.3CoCrFeNi high entropy alloy. *Mater Design* **121**, 254-260 (2017).
7. T. Pollock, J. Dibbern, M. Tsunekane, J. Zhu, A. Suzuki, New Co-based γ-γ' high-temperature alloys. *Jom-Us* **62**, 58-63 (2010).
8. K. Kumar, R. Sankarasubramanian, U. V. Waghmare, Influence of dilute solute substitutions in Ni on its generalized stacking fault energies and ductility. *Computational Materials Science* **150**, 424-431 (2018).
9. J. Lu *et al.*, Stacking fault energies in austenitic stainless steels. *Acta Materialia* **111**, 39-46 (2016).
10. B. H. Kear, J. M. Oblak, A. F. Giamei, Stacking faults in gamma prime Ni 3 (Al, Ti) precipitation hardened nickel-base alloys. *Metallurgical Transactions* **1**, 2477 (1970).
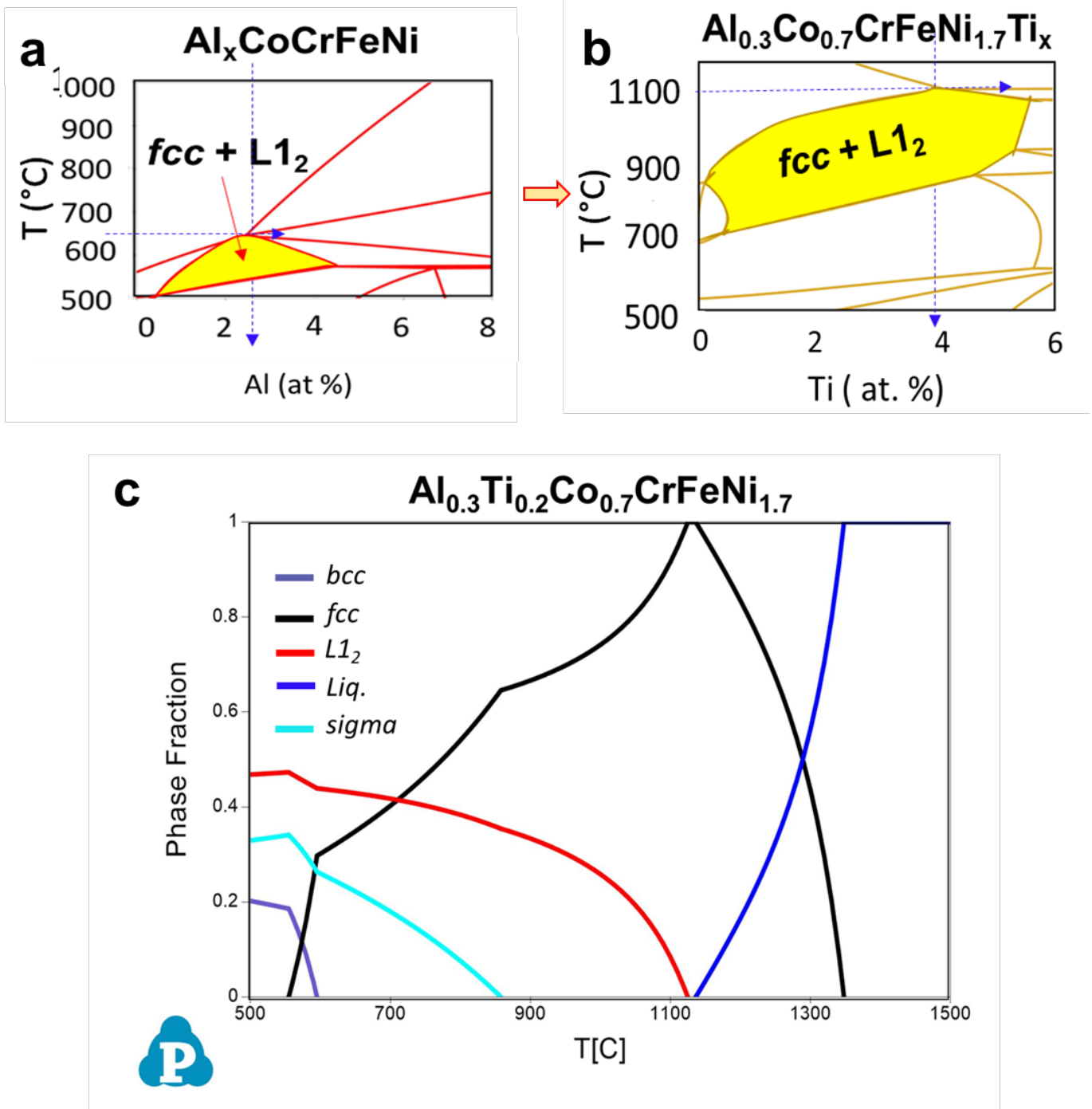
Deformation Twinning in a Metal-Intermetallic System: Novel Paradigm for Designing Alloys with Exceptional Strength-Ductility Combination

Bharat Gwalani[a#], Sriswaroop Dasari[a], Vishal Soni[a], Abhinav Jagetia[a], Shivakant Shukla[a], Priyanshi Agrawal[a], Rajiv S. Mishra[a], Rajarshi Banerjee[a]

[a]Materials Science and Engineering, University of North Texas, Denton, TX 76207
[#]current address: Physcial and Computational Directorate, Pacific Northwest National Laboratory, 902, Battelle Blvd, Richland, WA 99354
Corresponding authors: bharatgwalani@my.unt.edu, raj.banerjee@unt.edu

Figure 1: CALPHAD based alloy design strategy for the ultra-high strength HEA. (a) Optimizing Al content based on the isopleth showing phase stability as a function of temperature and Al mole percent in a CoCrFeNi base alloy. (b) Optimizing Ti content in $Al_{0.3}Co_{0.7}CrFeNi_{1.7}$ base alloy for high temperature phase stability of intermetallic $L1_2$ phase. The base alloy was chosen based on the most favorable Co, Cr, Fe and Ni content for a high temperature high strength microstructure (refer to Fig. S1). (c) The phase fraction vs temperature plot for the resultant ultra-high strength HEA.
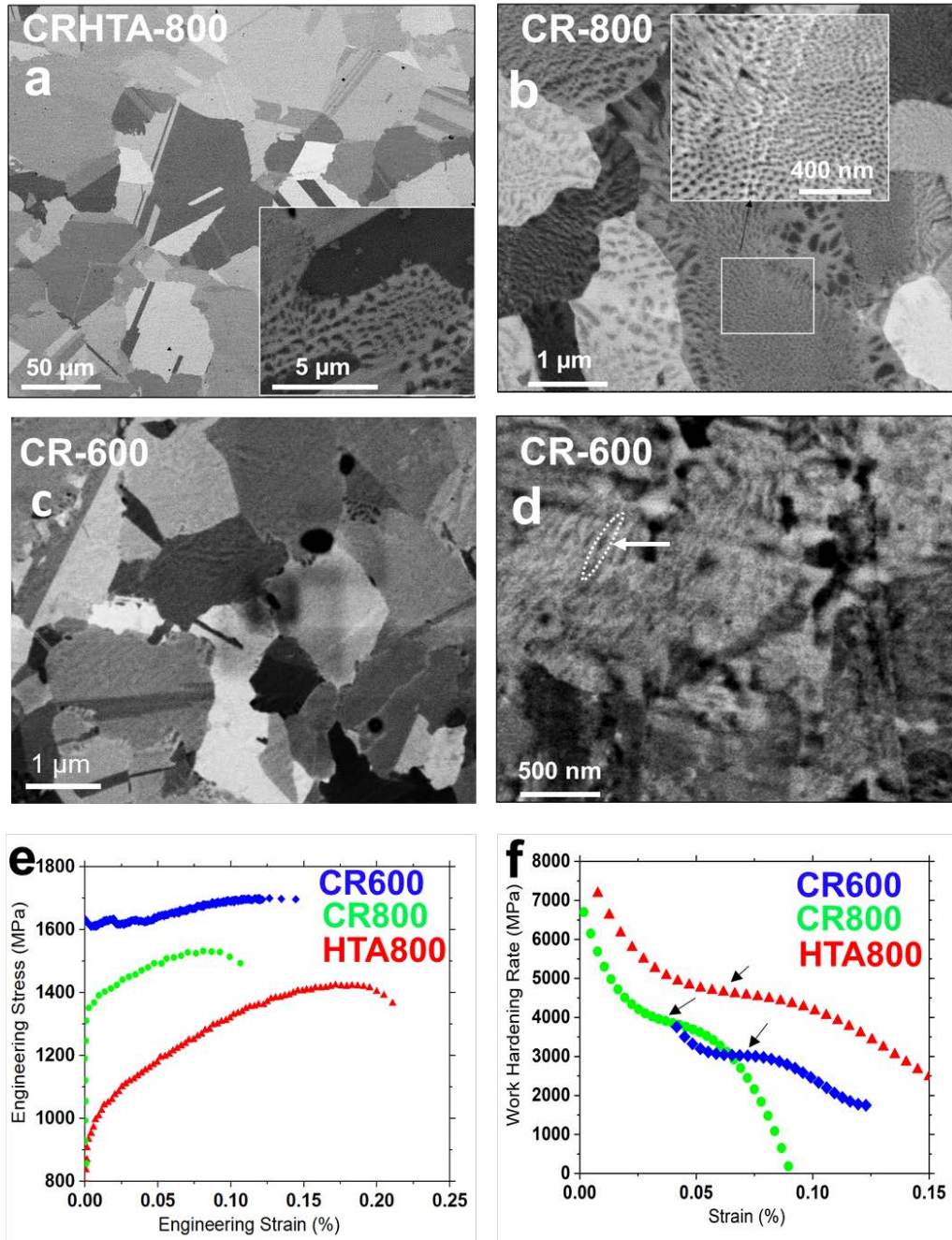
Figure 2: (a) The coarse recrystallized FCC grain structure in CR-HTA-800 condition. A high magnification picture revealing spherical/ellipsoidal precipitation within the grains is provided in the inset. (b) The fine grain structure in CR-800 and the change in precipitate morphology from lamellar at the grain boundaries to spherical in the interior of the grains (inset). (c) Ultra-fine grain structure of CR-600 condition (d) A high magnification picture of CR-600 condition showing nano-lamellar precipitation within the ultra-fine grains. (e) The tensile engineering stress vs strain curves for CR-HTA-800, CR-800 and CR-600 conditions. (f) Work-hardening plots for the three conditions revealing multi-stage hardening mechanisms activated as a function of plastic strain.
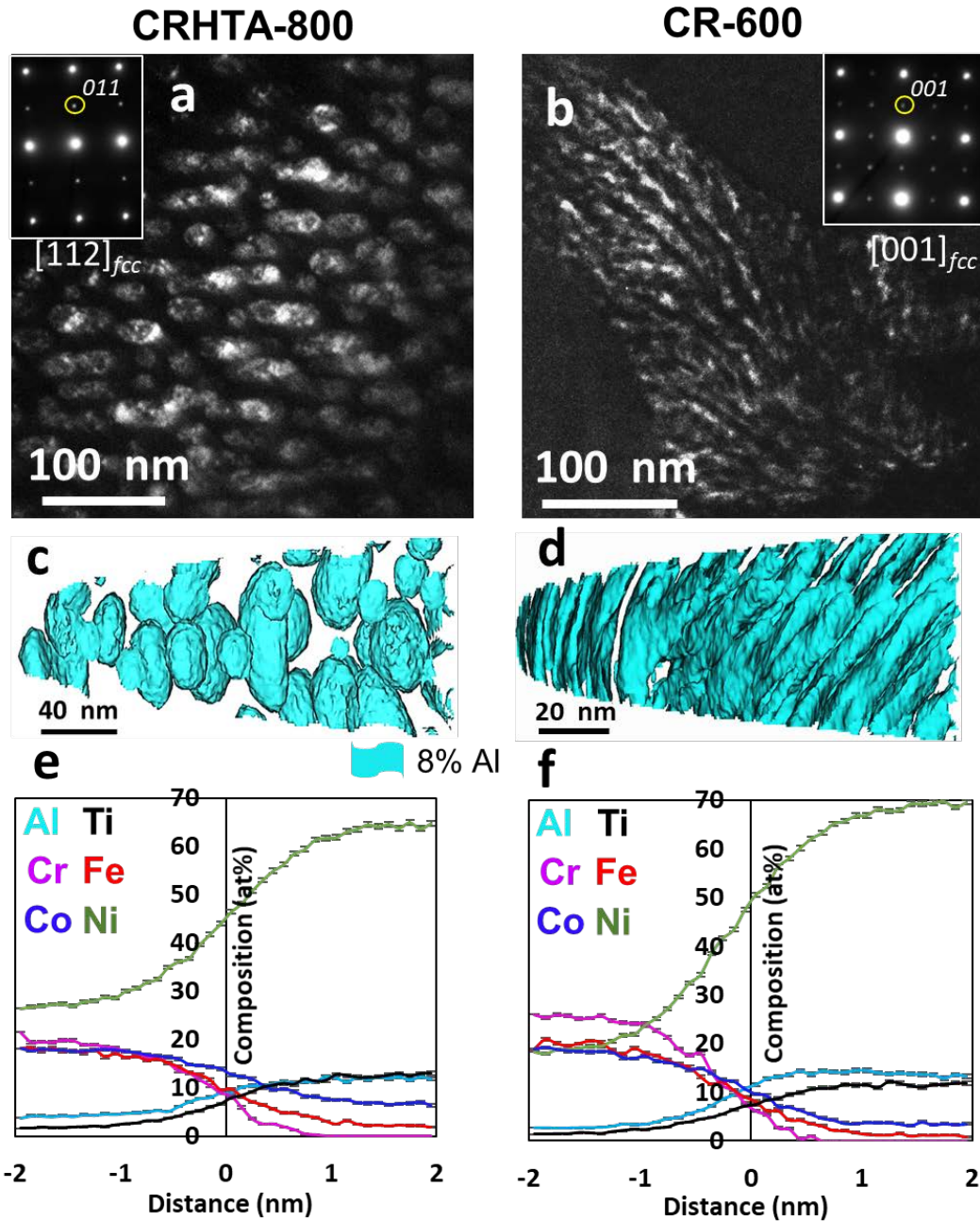
Figure 3: The crystal structure, morphology and composition of precipitates in CR-HTA-800 and CR-600 conditions that explains the trend in tensile yield stress. (a) Dark Field TEM micrograph showing spherical/ellipsoidal L12 precipitates in CR-HTA-800 condition recorded from {011} superlattice reflection in the diffraction pattern (inset) taken from [112] FCC zone axis. (b) Dark Field TEM micrograph showing nano-lamellar L12 precipitates in CR-600 condition recorded from {001 superlattice reflection in the diffraction pattern (inset) taken from [001] FCC zone axis. (c) The 3D APT reconstruction from CR-HTA-800 shows the morphology and distribution of L12 precipitates within the matrix. (d) The 3D APT reconstruction revealing the dense nano-layers of L12 phase within the FCC matrix in CR-600 condition; The proxigrams constructed across 8 at.%.
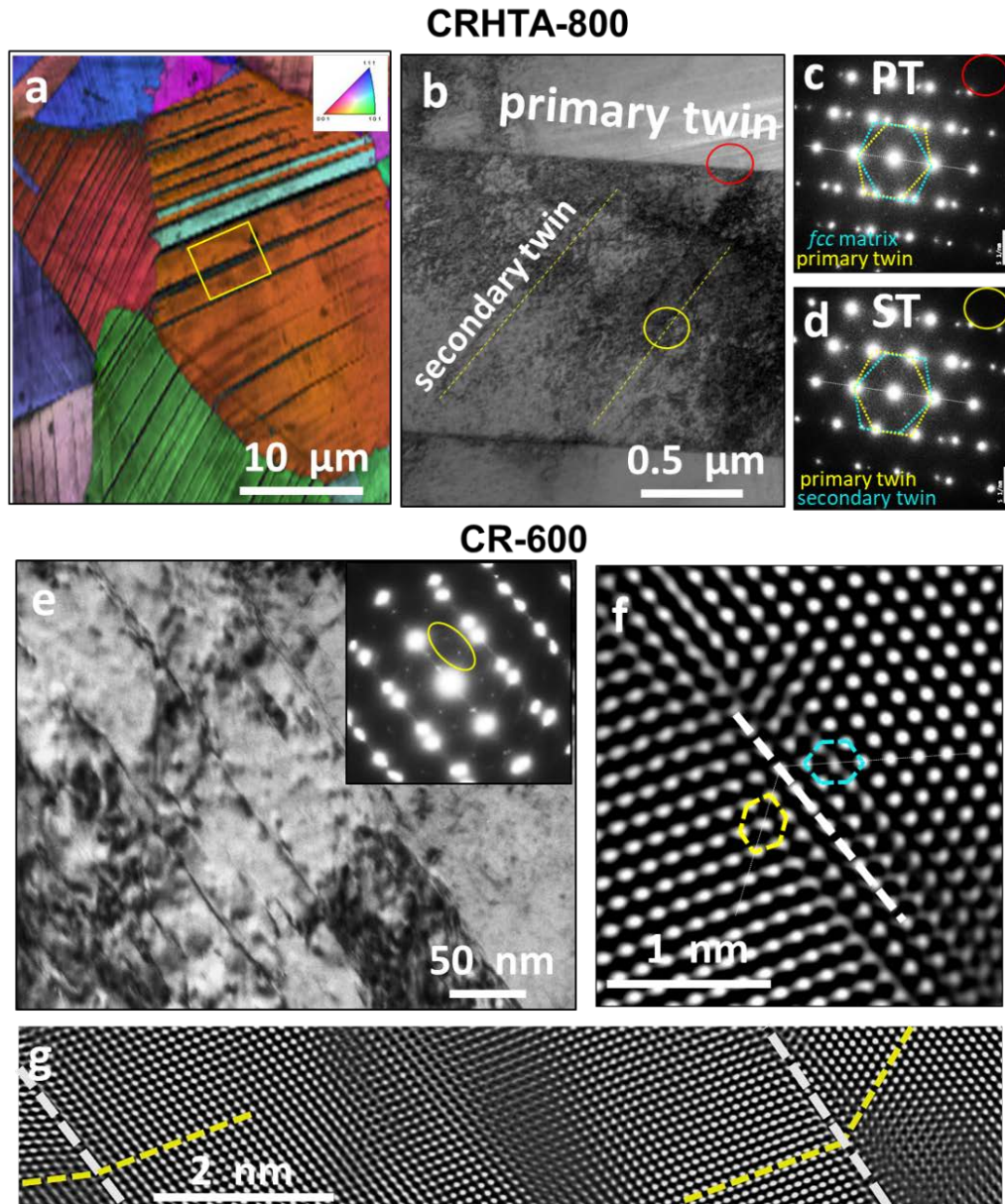
Figure 4: The deformation mechanisms in CR-HTA-800 and CR-600 conditions that explains the trend in multi-stage work-hardening. (a) IPF map overlaid on IQ map obtained from EBSD of CR-HTA-800 condition showing thick deformation twins in the matrix. (b) Hierarchical deformation twinning exhibited by CR-HTA-800 condition, primary twin is the darker contrast region and the secondary twins are highlighted with yellow dotted lines. (c) A diffraction pattern showing twin relation between the primary twin and the adjacent FCC grain (taken from red circle in (b)) (d) A diffraction pattern showing the twin relationship between primary and secondary twins (taken from yellow circle in (b)) (e) Bright field TEM micrograph obtained from the ultra-fine grained CR-600. Diffraction pattern in the inset shows the evidence for twinned L1$_2$ nano-

layers and FCC matrix; HAADF-STEM micrographs showing (f) a twin plane and (g) the thickness of twins in the ultra-fine-grained material.